TIME-FREQUENCY METHODS FOR THE ANALYSIS OF MULTISTATIC ACOUSTIC SCATTERING OF ELASTIC SHELLS IN SHALLOW WATER.

A Thesis
Presented to
The Academic Faculty

by

Shaun D. Anderson

In Partial Fulfillment
of the Requirements for the Degree
Master of Science in the
George W. Woodruff School of Mechanical Engineering

Georgia Institute of Technology
May 2011

TIME-FREQUENCY METHODS FOR THE ANALYSIS OF MULTISTATIC ACOUSTIC SCATTERING OF ELASTIC SHELLS IN SHALLOW WATER.

Approved by:

Professor Karim G. Sabra, Ph.D., Advisor
George W. Woodruff School of Mechanical Engineering
Georgia Institute of Technology

Professor Peter H. Rogers, Ph.D.
George W. Woodruff School of Mechanical Engineering
Georgia Institute of Technology

Principle Research Scientist David Trivett
George W. Woodruff School of Mechanical Engineering
Georgia Institute of Technology

Date Approved: December 2010

TABLE OF CONTENTS

LIST OF TABLES v

LIST OF FIGURES vi

LIST OF SYMBOLS OR ABBREVIATIONS xi

GLOSSARY xi

SUMMARY xi

I INTRODUCTION 1

1.1 Background 3

1.1.1 Fluid Loading Effects on Plates/Shell 3

1.1.2 Literature Review 5

1.2 Motivation and Goals 6

1.3 Thesis Organization 7

II METHODS 8

2.1 Shell Model 8

2.2 Quantitative ray theory for spherical shell 12

2.3 Time-frequency analysis with the Smooth Pseudo Wigner-Ville (SPWV) transform 16

2.3.1 Smoothing Window Selection 18

III MID-FREQUENCY ENHANCEMENT AND BISTATIC EFFECTS . . 21

3.1 Mid-frequency Enhancement 21

3.2 Effect of Environment and Shell Parameters on MFE 24

3.3 Time-frequency analysis of the bistatic evolution of spherical shell's scattered field 26

3.4 Physical interpretation of the time-frequency evolution of the bistatic MFE pattern from quantitative ray theory 29

IV APPLICATION TO TIME-FREQUENCY BEAMFORMING 34

V CONCLUSIONS 39

APPENDIX A MATLAB CODE 41
APPENDIX B MODAL EXPANSION COEFFICIENTS 60
REFERENCES 63

LIST OF TABLES

1 Shell Model Parameter Details 12

LIST OF FIGURES

1 Illustration of the Symmetric and Anti-symmetric wave modes that occur in a fluid loaded plate. The plate compression and expansion at each surface is shown by arrows. This depiction is taken from Fig. 8-15 in "Ultrasonic Waves in Solid Media"[18] 4

2 Schematic and ray diagram for the acoustic scattering problem under consideration. A plane-wave broadband pulse is incident from the left on a thin empty spherical shell immersed in water. The time-domain far-field bistatic scattering pressure is computed using a partial wave series (see Eq. 10). The ray diagram of the scattered field is also displayed for the specular reflection (dash dot line), and surface guided waves (dashed line) circumnavigating the shell and giving rise to the mid-frequency enhancement echo. The acoustic wave couples into the shell's wall at angle α-measured from the normal direction to the shell's wall - and radiates out towards a bistatic receiver (located at a distance r and azimuth angle θ) at the same angle α. 11

3 Bistatic ray diagrams for the subsonic A_{0^-} wave in the vicinity of the coincidence frequency for the (a) counter-clockwise or (b) clockwise propagating components. Note the difference in arc path angles ϕ_{cc} and ϕ_c for respectively the counter-clockwise or clockwise components (see Eq. (15-16)). The bistatic receiver is located at a distance r and azimuth angle θ. 12

4 Evolution of (a) Phase velocities, (b) Group velocities and (c) Radiation damping coefficients vs. normalized frequency ka for the anti-symmetric guided wave modes A_{0^+} (dashed line) and A_{0^-} (solid line)-adapted from Fig. B1 in Zhang et al.[34]. 14

5 Time-Frequency Representations of signal composed of two linear chirps spanning respectively the frequency bands 5-15kHz and 15-25kHz: (a) is Short Time Fourier Transform (b) Wigner-Ville distribution showing interference patterns between two signals (c) smoothed pseudo Wigner-Ville distribution. The SPWV distribution shows better time and frequency localization then the spectrogram and with reduced interference patterns inherent of the standard Wigner-Ville. 17

6 Overlay of standard amplitude smoothing windows including Hanning, Hamming, Blackman, Gauss, and Kaiser. Each window has length of 100 points, and the defining parameters of the Gaussian window and the Kaiser window were selected to be $\alpha = 0.005$, and $\beta = 3\pi$ respectively. 18

7 SPWV with different Hanning window sizes with double (wide) and half (narrow) the length of reference smoothing window (reference window sizes are 205 points in time and 171 points in frequency) (a) Narrow window in frequency domain (b) Narrow window in Time domain (c) Broad window in frequency domain (d) Broad window in time domain. 19

8 SPWV representation of shell response with appropriate smoothing window size based on empirical study. The Hanning windows used for smoothing were a time window of 0.2ms (205 points) in length and a frequency smoothing window of 192 Hz (171 points). 20

9 Impulse response of the spherical shell in the backscatter direction $\theta = 180°$ (computed from Eq. (10)) in the frequency band [1Hz-80kHz] using the physical parameters listed in Table 1. The displayed values were normalized by the maximum value of the specular echo. The three arrows indicate the specular echo -labeled (a)- and the echoes of the circumnavigating surface guided waves associated with the first symmetric modes (S_0, -labeled (b)-) and first antisymmetric mode (A_0, labeled (c)) which corresponds to the MFE. Subsequent arrivals correspond to surface guided waves undergoing multiple revolutions around the spherical shell. 21

10 Time-Frequency Representation showing the Fourier representation of the signal in the upper left corner, the time domain response of the signal in the lower right, and the SPWV Time-Frequency representation in the upper right. 23

11 SPWV representations of the first MFE echo for a spherical shell with two different material types (a) a Steel Shell and (b) same parameters as (a) but with shell made of Titanium. 24

12 SPWV time-frequency effects on MFE with changing parameters. (a) Reference shell using parameters listed in Table 1. (b) Same as (a) with radius of 0.61m, which lowers the center frequency and increases time between echo repetitions. (c) Same as (a) with a shell surrounded by gravel, which increases the radiated energy from S_0 wave. The parameters used for gravel are $C = 1800m/s$, $C_t = 716m/s$, $\rho = 2000kg/m^3$. 25

13 Evolution of the envelope (in logarithmic scale) of the bistatic impulse response of the spherical shell (computed with Eq. (10) using the model parameters listed in Table 1) vs. bistatic angle, θ. The amplitudes were normalized with respect to the maximum values of the scattered field in the monostatic (or backscatter) direction $\theta = 180°$. The first curved arrival corresponds to the specular echo. The two branches of the subsequent X-shaped pattern correspond respectively to the counter-clockwise ("cc" symbol) and clockwise ("c" symbol) propagating components of the A_0 mode. Note that the arrival-times of these two components differ for bistatic receivers (see Fig. 5), except for the monostatic direction $\theta = 180°$ their path around the spherical shell become symmetric with equal lengths. 26

14 Smoothed Pseudo-Wigner Ville representation (in logarithmic scale) of the impulse response of the spherical shell for three representative receiver's azimuth angles (a) monostatic direction $\theta = 180°$, or bistatic directions (b) $\theta = 135°$ and (c) $\theta = 90°$. The energetic MFE echo (due to the interference of the clockwise and counterclockwise propagating A_0 wave) in the monostatic direction is visible at time $t = 7.66ms$ (dashed vertical line) and a normalized frequency $ka = 46$ (dashed horizontal line). The bistatic configurations illustrate the progressive splitting of the MFE echo into two distinct clockwise and counterclockwise arrivals (see Fig. 3), as well as their relative time-frequency shift with respect to the monostatic echo. For each angle the magnitude were normalized by the maximum displayed value. 28

15 Variations of the arrival time of the MFE echo vs. bistatic receiver angle θ (see geometry in Fig. 3) with respect to the monostatic arrival time of the MFE (i.e. $\theta = 180°$). The triangle and circle symbols indicate the measured arrival times for respectively the clockwise and counter-clockwise A_{0^-} waves, as measured using the local maxima in the time-frequency plane of the smoothed pseudo Wigner-Ville representation of the bistatic scattered field (see Fig. 14). For comparison, the solid and dashed lines correspond to the arrival-times predicted from the ray synthesis for the same clockwise and counter-clockwise A_{0^-} waves. 30

16 Ray models of the amplitudes of the earliest counter-clockwise A_{0^-} wave arrival (based on the form function, $f_{l,m}$ given by Eq. (13) for $m = 0$) in the vicinity of the coincidence frequency for same three bistatic receiver angles θ shown in Fig. 14. Note the maximum of the amplitude's enhancement in the mid-frequency region progressively increases from $ka \approx 46$ at $\theta = 180°$ to $ka \approx 49$ at $\theta = 90°$. 31

17 Variations of the normalized center frequency of the MFE echo (i.e. coincidence frequency) vs. bistatic receiver angle θ (see geometry in Fig. 1) with respect to the monostatic arrival time of the MFE (i.e. $\theta = 180°$). The triangle and circle symbols indicate the center frequencies for respectively the clockwise and counter-clockwise A_0 arrival as measured from the local maxima in the time-frequency plane of the smoothed pseudo Wigner-Ville (SPWV) representation of the bistatic scattered field (see Fig. 3). The vertical error bar depicts the measurement resolution along the frequency axis on the SPWV representation, which accounts for most of the spread in the measured values. For comparison, the solid and dashed lines correspond to the center frequency of MFE echo predicted from the theoretical ray amplitude variations as shown on Fig. 16. 33

18 (a) Upper Panel: Stacked representation of the time-aligned arrivals of counter-clockwise propagating A_{0^-} waves (see Fig. 13) recorded at five different bistatic angles. The relative bistatic time-shifts, with respect to first bistatic angle $\theta_1 = 100°$ were obtained from the SPWV analysis (see Fig. 15). Lower Panel: Coherent addition of the five time-shifted waveforms using a conventional time-delay beamformer (computed by when setting the companding parameter as $\gamma_j = 1$- see Eq. (17)). (b) Upper Panel: same as (a), but each waveform was also companded to account for the apparent frequency shift of the bistatic counter-clockwise propagating A_{0^-} arrival-with respect to the first bistatic angle $\theta = 100°$- based on the measured frequency-shifts values from the SPWV analysis (see Fig. 17). Lower Panel: Coherent addition of the five time-frequency shifted waveforms using a generalized time-frequency beamformer (see Eq. (17)). Note that each bistatic waveform, in both upper panels, was normalized to its maximum value, such that one would expect a maximum beamformer output of 5 when an optimal coherent addition is achieved. 36

19 Schematic of the bistatic receivers layout around the spherical shell used for the numerical simulations (see Fig. 20). Each receiver array is centered on the monostatic direction-$\theta = 180°$-and is composed of an odd number N of receivers which are uniformly spaced in azimuth angle at 1° apart. 37

20 Evolution of the maximum value of the array beamformer $B(t;N)$ (see Eq. (17)) for increasing number of receiver N (equivalent here to an increasing angular aperture of the receiver array see Fig. 19). Asterisk and dot symbols mark respectively the values obtained the conventional time-delay beamformer formulation (i.e. when the companding (or time-scaling) parameter is set to $\gamma_j = 1$) or the generalized time-frequency beamformer formulation. The linear dependency of the number of N of receiver (dashed line) is also added for comparison and corresponds to the optimal achievable value of the array beamformer output $B(t;N)$ when the arrivals of counter-clockwise propagating A_0–waves recorded by the N receivers add in phase coherently. 38

21 Modal Expansion coefficients taken from Eq.(6a) and Eq. (6b) in Goodman and Stern [6]. 61

22 Additional details of Modal Expansion coefficients taken from Eq.(6a) and Eq. (6b) in Goodman and Stern [6]. 62

SUMMARY

The development of low-frequency sonar systems, using for instance a network of autonomous systems in unmanned vehicles, provides a practical means for bistatic measurements (i.e. when the source and receiver are widely separated) allowing for multiple viewpoints of the target of interest. Time-frequency analysis, in particular Wigner-Ville analysis, takes advantage of the evolution time dependent aspect of the echo spectrum to differentiate a man-made target (e.g. elastic spherical shell) from a natural one of the similar shape (e.g. solid). A key energetic feature of fluid loaded and thin spherical shell is the coincidence pattern, or mid-frequency enhancement echoes (MFE), that result from antisymmetric Lamb-waves propagating around the circumference of the shell. This thesis investigates numerically the bistatic variations of the MFE (with respect to the monostatic configuration) using the Wigner-Ville analysis. The observed time-frequency shifts of the MFE are modeled using a previously derived quantitative ray theory for spherical shell's scattering [35]. Additionally, the advantage of an optimal array beamformer, based on joint time delays and frequency shifts (over a conventional time-delay beamformer) is illustrated for enhancing the detection of the MFE recorded across a bistatic receiver array.

CHAPTER I

INTRODUCTION

Detecting and classifying proud or buried objects in shallow water is a challenging problem with high practical importance. Some applications for this problem include, but are not limited to; mine countermeasures (MCM) harbor protection; pipeline maintenance; buried waste retrieval as well as underwater archeology [2]. In the context of low-frequency active sonar, a key interest for MCM applications is the ability to distinguish acoustic echoes of man-made targets (e.g. elastic shell) from ocean reverberation (e.g. due to bottom or volume scattering) and ambient noise, especially in the presence of multipath [10]. In particular, time-frequency analysis has been shown to be a relevant tool for the acoustic detection and classification of elastic shells and propagation in dispersive media [5, 33, 30].

Furthermore, the development of MCM sonar systems, for instance using a network of autonomous systems in unmanned vehicles, provides a practical means for bistatic measurements (i.e. when the source and receiver are widely separated) allowing for multiple viewpoints of the target of interest [10, 16]. Such systems can potentially yield bistatic enhancement for detection and classification capabilities when compared to traditional monostatic systems (i.e. where the source and receivers are co-located or closely spaced) [10, 16]. Consequently, in order to design optimum receiver and signal-processing algorithms for such bistatic sonar systems, it is then fruitful to understand the spatial and temporal variations of the bistatic acoustic scattering responses of elastic shells.

The physics of acoustic scattering from elastic shells with simple shapes, such as spheres or infinite cylinders, has been extensively studied both theoretically and

experimentally [14, 17, 22, 25]. The main motivation of those studies is to develop a precise description of the mechanisms of echo formation, in order to accurately describe the physical features of acoustic scattering. In particular, a practical goal is to identify acoustic features unique to elastic shells (i.e. man-made objects) and how these acoustic features change with a particular source-target-receiver geometry in order to ultimately use these acoustic features for classification purposes. As shown schematically in Fig. 2, a fluid loaded thin spherical shell produces a specular or direct reflection (similar to any acoustically reflective hard object of comparable shape) as well as guided waves (or Lamb waves) circumnavigating the shell. Consequently, for traditional monostatic systems, a key energetic feature of a spherical shell is the mid-frequency enhancement echo (MFE)-also called the coincidence pattern- that is created by the coherent addition of the first antisymmetric Lamb waves (A_0 mode) propagating clockwise and counterclockwise around the shell. This MFE yields energetic acoustic echoes radiating in the surrounding fluid and thus provides a unique acoustic signature of fluid loaded spherical shells, as previously demonstrated theoretically and experimentally (e.g. See Fig. 9)[14, 22, 34].

For instance, the frequency band of the MFE and the temporal spacing between successive circumnavigating Lamb waves allows an estimate of the radius of the spherical shell [24] as well as the shell material properties [13, 31]. Most time-frequency analysis of the MFE have focused on source-receiver configuration close to monostatic (i.e., when source and receiver are co-located in azimuthal angle with respect to the shell's centroid) where the MFE is most energetic [8, 9, 13]. The MFE persists for bistatic configurations and thus still carries information about the physical features of the elastic shell (e.g. see Fig. 13). However, a practical challenge of utilizing the bistatic measurement is the significantly reduced amplitude of the bistatic MFE compared to monostatic measurements. This renders the MFE detection more difficult in the presence of high clutter or ambient noise levels. Consequently, bistatic detection

of the MFE would need to be enhanced, for instance by combining the signals measured on an array of receivers using array beamforming techniques [12]. The design of an optimal beamformer for MCM applications should be determined by the specific time-frequency coherence of the bistatic MFE echoes in order to allow for an optimal coherent addition of these echoes across a bistatic aperture [26].

The main goal of this thesis is to investigate theoretically and numerically the bistatic variations of the MFE for a thin spherical shell that is fluid loaded utilizing time-frequency analysis. This canonical target shape was selected as its acoustic scattered field and echo generation mechanism is well documented and understood. The acoustic scattered field is computed from a modal expansion whose coefficients are determined by the shell's physical properties and appropriate boundary conditions at the fluid interface using the classical formulation of Goodman and Stern [6]. Time-frequency analysis of the most energetic bistatic echoes, associated with the circumnavigating anti-symmetric Lamb waves, is performed using the Smoothed Pseudo Wigner-Ville transform.

The main contribution of this thesis is to quantify the dependence of the time-frequency shifts of the MFE on the bistatic receiver angles and explain the observed time-frequency shifts using a previously derived quantitative ray theory for scattering by a spherical shell [35]. Additionally, an array beamformer based on joint time-frequency shifts is demonstrated to outperform a conventional time-delay beamformer for enhancing the bistatic detection of the MFE for spherical shells.

1.1 Background

1.1.1 Fluid Loading Effects on Plates/Shell

The basic physical principles that are involved in the formulation of the scattered field from a spherical shell are similar to those found when investigating a fluid loaded plate. In such an instance, there are a combination of flexural and compressional

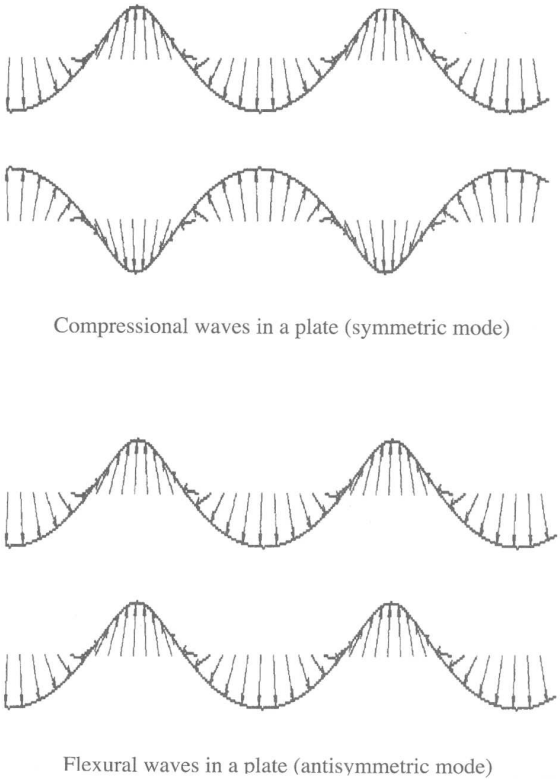

Figure 1: Illustration of the Symmetric and Anti-symmetric wave modes that occur in a fluid loaded plate. The plate compression and expansion at each surface is shown by arrows. This depiction is taken from Fig. 8-15 in "Ultrasonic Waves in Solid Media"[18]

waves formed, which can be separated into Anti-symmetric and Symmetric modes. The zero order Antisymmetric mode (A_0) and Symmetric mode (S_0) exist over the entire frequency range and typically carry more energy then higher order modes. These two types of modes in a plate are depicted in Fig. 1. The solutions for these modes are well understood and the vibrational behavior of a flat plate can be calculated using the Rayleigh-Lamb equations [1]. In particular, the interaction of the flexural and compressional waves can create a phenomenon called a leaky Lamb mode, which radiates energy from the plate into the surrounding fluid medium. These are the modes of interest for MCM purposes, due to the energy being 'leaked' into the outer fluid medium. Additionally this physical behavior can now be extended to a thin shell in which the plate is simply wrapped up into a sphere. Thus the behavior

is no longer the true definition of a Lamb mode (since it is no longer occurring on an infinite flat plate), and is why the literature sometimes refers to these waves as Lamb-type modes.

1.1.2 Literature Review

The examination of the mid-frequency enhancement feature has been extensively studied in articles covering a variety of spherical and cylindrical shells[8, 9, 13, 14, 17, 22, 25, 34]. Both theoretical and experimental analyses of fluid loaded shells were reported. Many papers on this topic can be traced back to the closed form solution model presented by Goodman and Stern. The canonical form of this solution and extensive literature published for a spherical shell makes this shape an obvious choice for theoretical analysis of the MFE using time frequency analysis [6]. Further work was done by Felsen and Ho, in which exact and approximate formulations of fully three-dimensional model of the scattered field from a spherical shell surface were presented [4, 7].

One interesting phenomenon which occurs within the shell was presented by Sammelmann et al. in which the dispersion curve of the lowest anti-symmetric mode was shown to bifurcate into two waves; a shell-borne and a fluid-borne wave, which interact to create the MFE echo [19]. These two lowest order anti-symmetric modes are commonly noted by the positive and negative indices, A_{0^-} and A_{0^+}, which is used to indicated there opposite nature.

Additionally, papers written by Talmant, Zhang, and Marston [14, 22, 34] covered a variety of experiments, and ray modeling techniques to better understand the MFE phenomenon with respect to differing types of excitation. These ray techniques will be addressed further in the following chapter. Recently the MFE was studied in a paper by Li [11] in which it was shown that the repetition and frequency of the MFE could be used to estimate the radius and thickness of a shell for classification purposes.

Though these articles investigate the formation mechanism of the MFE, none expand on the MFE features measured in a bistatic setup. Instead, previous literature primarily focused on the backscatter (monostatic) direction, which is the most energetic direction for this feature due to the symmetry of the sphere and coherent addition of clockwise and counter-clockwise circumnavigating waves. The bistatic behavior is mentioned briefly in papers by Marston, Sun, and Zhang [14, 15, 21, 34], but little attention is given to the time-frequency content of the MFE.

1.2 Motivation and Goals

As previously mentioned the motivation of this work is to be able to utilize unique acoustic features of a man-made object in order to detect and classify the object based on its structural response to acoustic excitation. The MFE is an obvious choice due to its characteristics and highly energetic signal for spherical and cylindrical shells. These shapes are used as a first order approximate model for mines and thus the obvious appeal for MCM applications. Additionally the motivation of this work is to lay groundwork and gain better understanding on the optimal way to process acoustic echoes collected in a bistatic source and receiver setup. This motivation for optimal processing of bistatic data comes from the advance and greater use of autonomous underwater vehicles (AUVs). The deployment of multiple AUVs into an area allows the collection of several bistatic viewpoints of the area. The practical problem is how to process this bistatic data. The traditional thought is to use a moving source and receiver as a synthetic array, in which one can create a virtual array along the AUV path and use optimal array processing techniques to image an area, and or locate targets (e.g. as used in Synthetic Aperture Sonar). This type of target searching method with multiple AUVs allows greater area coverage when compared to a single vessel as a source with a towed array. Each pulse from the source can now be collected on multiple receivers at different viewpoints simultaneously. Additionally by taking

advantage of synthetic aperture processing, the method does not require deployment of physically large arrays.

The goal of this research is to study the MFE of a spherical shell, draw conclusions about the usefulness of this acoustic feature for classification purposes and to determine a method that may be used to enhance the signal of an MFE using bistatic data. This particular problem of the MFE response with different source and receiver locations may seem trivial on an axisymmetric object, however the wave interactions of the antisymmetric lamb modes responsible for the MFE create a complex response. It will be shown in this thesis, that this response changes in time and frequency, which is a function of the angular separation of the source and receiver. Thus combining receiver data from various bistatic angles requires more attention than is immediately obvious. The outcome of this research would be to identify how the MFE varies with source-receiver configuration. Consequently, one would gain the ability to predict this bistatic MFE behavior in order to optimally process bistatic data to enhance the MFE extraction from noisy recordings for classification purposes.

1.3 Thesis Organization

This thesis is divided into six chapters. Chapter II presents the methods including the theoretical shell model used for computing the acoustic scattering from a spherical shell along with the Wigner-Ville formulation used to analyze the time-frequency content of the bistatic MFE. Additionally, chapter II contains a physical interpretation of the MFE using a quantitative ray interpretation to explain the observed time-frequency shifts of the bistatic MFE arrival. Chapter III investigates the bistatic evolution of the MFE arrival in the time and frequency domains. Chapter IV develops a generalized time-frequency beamformer formulation to coherently process MFE echoes recorded along a bistatic sensor array, based on the previous findings. Finally, chapter V summarizes the findings and conclusions drawn from this study.

CHAPTER II

METHODS

2.1 Shell Model

The scattered field of a thin fluid-loaded elastic spherical shell is computed using the classical theoretical formulation of Goodman and Stern[6] as described hereafter. Assuming that an incident harmonic plane wave with amplitude P_0 and frequency ω impinges on a shell in a homogeneous free space medium with sound speed c_0, the harmonic scattered field, $P(r, \theta, t)$, recorded at a receiver may be decomposed into a modal expansion. The inclination angle of the sphere is taken to be equal to zero because it is not of particular concern in this study due to the azimuthal symmetry of the sphere excited by a plane wave. Thus, the response calculations presented may be applied for any selected inclination angle. The general equations and process for this modal expansion will be reviewed here to set a basis for the research to follow. This work summarizes the formula of the Goodman and Stern paper for a spherical shell in free space[6].

In this approach, the displacement $\boldsymbol{u}$ is first expressed in terms of a scalar potential $\boldsymbol{\phi}$ and the vector potential $\boldsymbol{\psi}$: $\boldsymbol{u} = \nabla\phi + \boldsymbol{\nabla} \times \boldsymbol{\psi}$ [1]. Additionally the use of the linearized Euler equation will allow the acoustic pressure to be determined from the velocity via the displacement.

Using the decomposition of the displacement into scalar and vector quantities allows the equation of motion to be easily satisfied by two separate wave equations as follows.

$$(\frac{1}{C_L^2})(\frac{\partial^2\phi}{\partial t^2}) = \nabla^2\phi \tag{1}$$

$$(\frac{1}{C_T^2})(\frac{\partial^2\psi}{\partial t^2}) = -\boldsymbol{\nabla}\times\boldsymbol{\nabla}\times\psi \tag{2}$$

Where $C_L = [(\lambda+2\mu)/\rho]^{(1/2)}$ and $C_T = (\mu/\rho)^{(1/2)}$ are the longitudinal and transverse wave speeds, respectively, given in terms of density ρ and Lamé's constants λ and μ. The problem can then be broken down further for each medium of interest numbered as shown in Fig. 2. To simplify the representation the index, i will indicate each of the three mediums. Now taking the wave-numbers, k to be the angular frequency divided by the respective wave speed results in Eq. (3) and Eq. (4).

$$k_{i,L}^2 \equiv \frac{\omega^2\rho_i}{\lambda_i+2\mu_i} \tag{3}$$

$$k_{i,T}^2 \equiv \omega^2\frac{\rho_i}{\mu_i} \tag{4}$$

Then expressing each equation in terms spherical coordinates and assume a harmonic time dependence of $e^{-j\omega t}$ before taking the time derivative, and substituting the wave-numbers results in Eq. (5) and Eq. (6) for the potential functions.

$$(\nabla^2 + k_{i,L}^2)\phi_i = 0 \tag{5}$$

$$\frac{1}{r^2}\frac{\partial}{\partial r}\left(r^2\frac{\partial\Psi_i}{\partial r}\right) + \frac{1}{r^2}\frac{\partial}{\partial\theta}\left[\frac{1}{\sin\theta}\frac{\partial}{\partial\theta}\sin\theta\Psi_i\right] = -k_{i,T}^2\Psi_i \tag{6}$$

The modal form of the solutions, Ψ_i and ϕ_i, for these wave equations are the typical Bessel functions j_l and Legendre polynomials P_l that appear when solving partial differential equations in spherical coordinates. Where l is the mode number, and θ is the azimuthal angle on the shell, which is the only angle of importance in the measurement due to the problem symmetry (see Fig. 2):

$$\phi_i = \sum_{l=0}^{\infty} P_l(\cos\theta)[A_l^i j_l(k_{i,L}r) + B_l^i P_l(k_{i,L}r)] \tag{7}$$

$$\Psi_i = \sum_{l=0}^{\infty} \frac{\partial}{\partial \theta} P_l(\cos\theta)[C_l^i j_l(k_{i,T} r) + D_l^i P_l(k_{i,T} r)] \tag{8}$$

Finally, the appropriate boundary conditions must be applied to define the coefficient constants $A_l^i, B_l^i, C_l^i, D_l^i$. The boundary conditions for this problem are matching displacements and normal stresses at the interfaces, and setting tangential stress to be zero in the fluid domain, which allows one to obtain values for these coefficients. In this study, the concern is only with the acoustic response in the outer fluid (i.e. only the pressure field). Hence, the ϕ_1 term is the only one of importance, and therefore only the A_l^1 needs to be computed. This ϕ_1 term can be written as:

$$\phi_1 = \sum_{l=0}^{\infty} P_l(\cos\theta) A_l^1 h_l(k_{1,L} r) \tag{9}$$

Where h_l is the Hankel function (Bessel function of the third kind). The scattered field of a thin fluid-loaded elastic spherical shell can then be computed using the modal expansion of scalar displacement in Eq. 9. Assuming that an incident harmonic plane wave with amplitude P_0 and frequency ω impinges on a shell then the harmonic scattered field $P(r, \theta, t)$ [recorded at a receiver located in polar coordinates at (r, θ) (see Fig. 2)] is decomposed into the modal expansion:

$$P(r, \theta, t) = P_0 e^{-i\omega t} \sum_{l=0}^{\infty} i^l (2l+1) A_l^1 h_l^{(1)}(kr) P_l(\cos\theta) \tag{10}$$

Therefore each modal contribution involves the Hankel function of the first kind $h_l^{(1)}(x)$, and Legendre polynomial, $P_l(x)$, and $k = \omega/c_0$ is the acoustic wavenumber in the outer medium. Furthermore, the modal coefficients A_l^1 are determined by the appropriate boundaries conditions (i.e. continuity of constraints and displacements) at the interfaces separating the outer (1), shell (2), and inner (3) mediums as numbered in Fig. 2. Table 1 lists the selected physical properties for the numerical simulations which are representative for the elastic shells and surrounding fluid media with no attenuation for a 1.06m diameter hollow steel shell (thickness=26.5mm) immersed

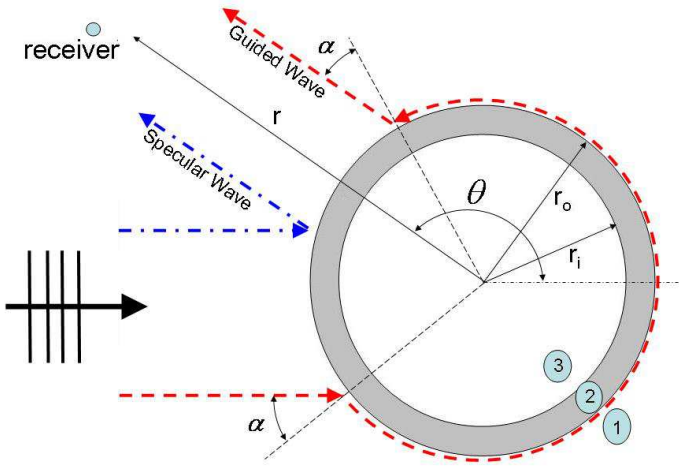

Figure 2: Schematic and ray diagram for the acoustic scattering problem under consideration. A plane-wave broadband pulse is incident from the left on a thin empty spherical shell immersed in water. The time-domain far-field bistatic scattering pressure is computed using a partial wave series (see Eq. 10). The ray diagram of the scattered field is also displayed for the specular reflection (dash dot line), and surface guided waves (dashed line) circumnavigating the shell and giving rise to the mid-frequency enhancement echo. The acoustic wave couples into the shell's wall at angle α-measured from the normal direction to the shell's wall - and radiates out towards a bistatic receiver (located at a distance r and azimuth angle θ) at the same angle α.

in water. These physical parameters were selected to be identical to those used by Zhang et al. [34] in order to ease the subsequent analysis of the MFE mechanism. Numerical simulations were conducted in the frequency band [1Hz-80kHz] and time-series were generated using Fourier synthesis of the harmonic solution given by Eq. (10). In particular, the modal sum was truncated arbitrarily at a mode index of $l = 100$ based on convergence tests: the amplitude's contribution of the higher-order modes ($l > 100$) were found not to significantly contribute to the amplitude of the synthesized broadband time-series.

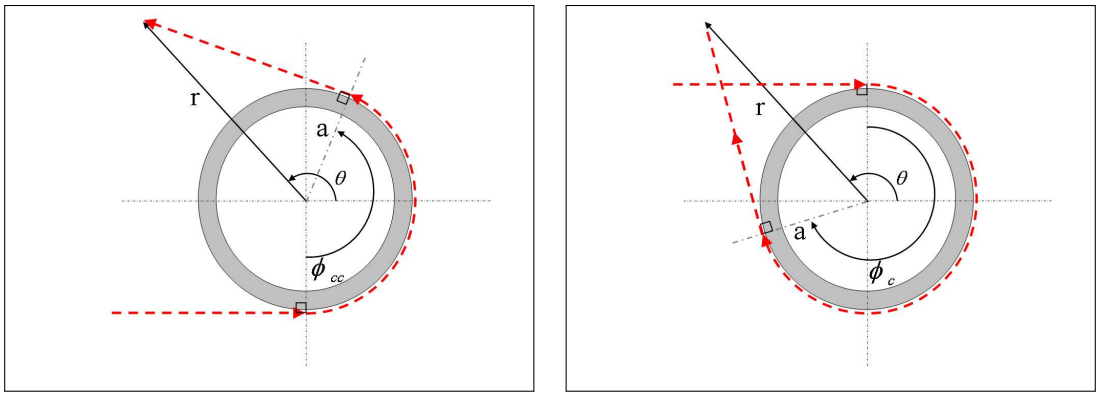

(a) (b)

Figure 3: Bistatic ray diagrams for the subsonic A_{0^-} wave in the vicinity of the coincidence frequency for the (a) counter-clockwise or (b) clockwise propagating components. Note the difference in arc path angles ϕ_{cc} and ϕ_c for respectively the counter-clockwise or clockwise components (see Eq. (15-16)). The bistatic receiver is located at a distance r and azimuth angle θ.

2.2 Quantitative ray theory for spherical shell

Extensive literature has been published on quantitative ray theory approximation for scattered field from elastic targets of various shapes [14, 28]. Consequently, only a short summary of the quantitative ray theory applied to a spherical shell is presented. This approximate ray analysis provides a physical basis for an intuitive interpretation of the different echoes (including the specular, A_{0^-}, A_{0^+}, S_0 arrivals) visible on the simulated bistatic time-series (e.g. see Fig. 9 and Fig. 13). In general, the geometric approach associates an individual ray component with each of the various specular and guided surface wave components within the shell (shown qualitatively on Fig.

Table 1: Shell Model Parameter Details

Parameter	Shell	Outside	Inside
Material	304 Stainless Steel	Water	Air
Density (ρ)	7570 kg/m^3	1000 kg/m^3	0.0013 kg/m^3
Longitudinal Wave Speed (C_L)	5675 m/s	1470 m/s	331 m/s
Transverse Wave Speed (C_T)	3141 m/s	0 m/s	0 m/s

2). This simple ray theory has been shown to be quantitatively accurate [14, 28] and only needs a slight correction in the forward scatter direction (i.e. $\theta \approx 0°$) to account for forward diffraction effects around the shell [9]. The arrival time of each ray component can be computed from a geometric calculation of its path length around the shell and within the surrounding medium (shown in Fig. 3 for A_{0^-} clockwise and counterclockwise paths).

Furthermore, the quantitative ray analysis presented hereafter will focus on the most energetic MFE which correspond to the interference of the A_{0^-} and A_{0^+} wave components (as discussed in chapter 3.1). In particular, based on the matched boundary conditions at the interface between the shell's wall and the surrounding medium, the angle of incidence α (with respect to the normal of the shell's surface as shown in Fig. 2) for the associated ray with either of the A_0 wave components, A_{0^-} and A_{0^+}, is determined by Eq. (11).

$$\sin(\alpha(f_c)) = \frac{C_0}{C_{phase}(f_c)} \tag{11}$$

Where f_c is the frequency of the harmonic excitation, C_0 is the sound speed of the surrounding homogeneous liquid and $C_{phase}(f_c)$ is the frequency-dependent phase velocity of either A_0 wave component (see Fig. 4(a)). The dispersion curves for the various waves, are determined from the same determinates used to calculate the modal coefficients, A_l^1, discussed in the previous section. Note that the angle, α, is also the launch angle of the A_0 ray radiating out while it circumnavigates the shell (see Fig. 2). Based on the selected parameters for the elastic shell (see Table 1) it can be noted that the phase velocities of the A_{0^-} and A_{0^+} components approach the value of the sound velocity of the surrounding fluid $C_0 = 1470m/s$ (see Fig. 2), near the coincidence frequency (i.e. where the MFE occurs $ka \approx 46$). Additionally the group velocity curves of the A_{0^-} and A_{0^+} components intersect (see Fig. 4(b)), which indicates an efficient energy coupling and strong constructive interference of the A_{0^-}

and A_{0+} components, as reported earlier [34].

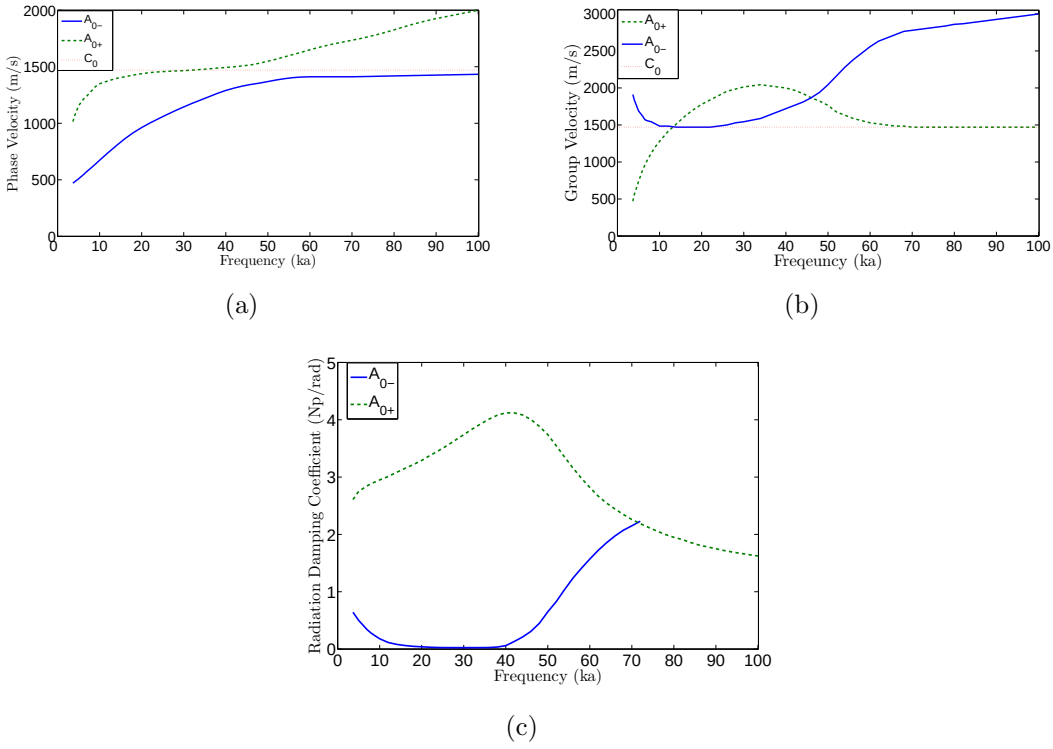

Figure 4: Evolution of (a) Phase velocities, (b) Group velocities and (c) Radiation damping coefficients vs. normalized frequency ka for the antisymmetric guided wave modes A_{0+} (dashed line) and A_{0-} (solid line)-adapted from Fig. B1 in Zhang et al.[34].

Previous developments of the quantitative ray theory approximation can be used to predict the amplitude variations of the A_{0-} and A_{0+} components in the vicinity of the MFE [34]. Again assuming that an incident harmonic plane wave with amplitude P_0 and frequency ω impinges on a shell in a homogeneous free space medium with sound speed c_0, the harmonic scattered field, $P(r, \phi, t)$, recorded at a range r is expressed as a superposition of the various ray components.

$$P(r, \phi, t) = \frac{P_0}{r} e^{i(kr - wt)} \sum_{l}^{\infty} f_{l,m}(\phi) \tag{12}$$

Where the angle (ϕ) parameterizes the angle of the arc path of each l^{th} ray component (see Fig. 3), having each a complex amplitude $f_{l,m}(\phi)$ (commonly referred

to as the form-function based on Partial Wave series expansion from elastic theory). The second index $m = 0, 1, 2...$ denotes the number of full circumnavigations of the individual ray components around the spherical shell. In particular, the form function associated with the anti-symmetric A_0 Lamb waves (i.e. either the A_{0^+} or A_{0^-} components) can be approximated by Eq. (13) [34].

$$f_{l,m}(\phi) = B_l e^{i\eta_l} \beta_l e^{(-\phi\beta_l - 2\pi m\beta_l)} \tag{13}$$

Where B_l is a complex coupling coefficient (whose exact expression differs for the A_{0^+} or A_{0^-} component), η_l is a propagation related phase shift parameter and β_l (Np/rad) is the radiation damping parameter for the considered A_0 waves. The values for these coefficients are found from applying the Sommerfeld-Watson methodology to the exact partial wave series [8]. Physically speaking, the parameter η_l determines the arrival time of the A_0 waves, and the parameter β_l quantifies the ability of energy to radiate from the A_0 waves into the surrounding fluid while circumnavigating the spherical shell. Fig. 4(c) displays the frequency dependence of the radiation damping modal coefficients for the A_{0^+} or A_{0^-} waves computed using the shell's physical parameters stated in Table 1 (the curves were adapted from a previous study by Zhang et al. [34]). In the vicinity of the coincidence frequency (i.e. $ka \approx 46$) the radiation damping parameter of the A_{0^-} wave is significantly lower than the radiation damping parameter of the A_{0^+} wave. Consequently, this indicates that the A_{0^-} is radiating out most of the energy associated with the MFE. Therefore, the theoretical variations of the form function $f_{l,m=0}$, predicted from Eq. (13), and the geometric path length of the ray associated with the A_{0^-} wave will be used to quantify the observed time-frequency shift of the bistatic MFE arrival as observed in Chapter III (see Fig. 14).

2.3 Time-frequency analysis with the Smooth Pseudo Wigner-Ville (SPWV) transform

As mentioned in the introduction, the main goal of this thesis is to analyze the bistatic variations of the MFE for a fluid loaded thin spherical shell. Indeed, time-frequency analysis has been shown to be a relevant tool for analyzing the acoustic echoes of elastic shells for MCM purposes[5, 17, 32, 33, 30]. Traditionally, time frequency analysis is carried out using the Short Time Fourier Transform (STFT), or spectrogram, which is a linear time-frequency method. Nevertheless, the time-frequency resolution of the STFT method is inherently limited by the time-frequency uncertainty principle [20]: higher temporal resolution requires using a narrower time-window, which in turn reduces the achievable frequency resolution (and vice-versa). One potential improvement towards higher resolution in both time and frequency is to utilize quadratic (i.e. higher-order) time-frequency transform or Cohen class time-frequency representations such as the Wigner-Ville transform [3]. One remarkable property of the Wigner-Ville transform is the ability to have unbiased measurement of the group velocity of each echo component within a signal, while maintaining marginal computation (i.e. the integrals along the time and frequency domains are the powers of the signal in the respective domain) [32, 33]. Although the Wigner-Ville transform can provide an optimal localization of broadband and transient signals in the time-frequency plane, it is not readily used in practice as it generates interference patterns between multiple components of the signal, which can complicate the analysis of the results (see Fig. 5(b)). In this case, two simple linear chirps were superimposed and analyzed to illustrate the benefits of the Wigner-Ville transform even in a simple case.

For practical applications, it has been shown that a variant of the Wigner-Ville transform the Smoothed Pseudo Wigner-Ville transformation (SPWV) can be used to reduce these interference patterns, thus easing the physical identification of the

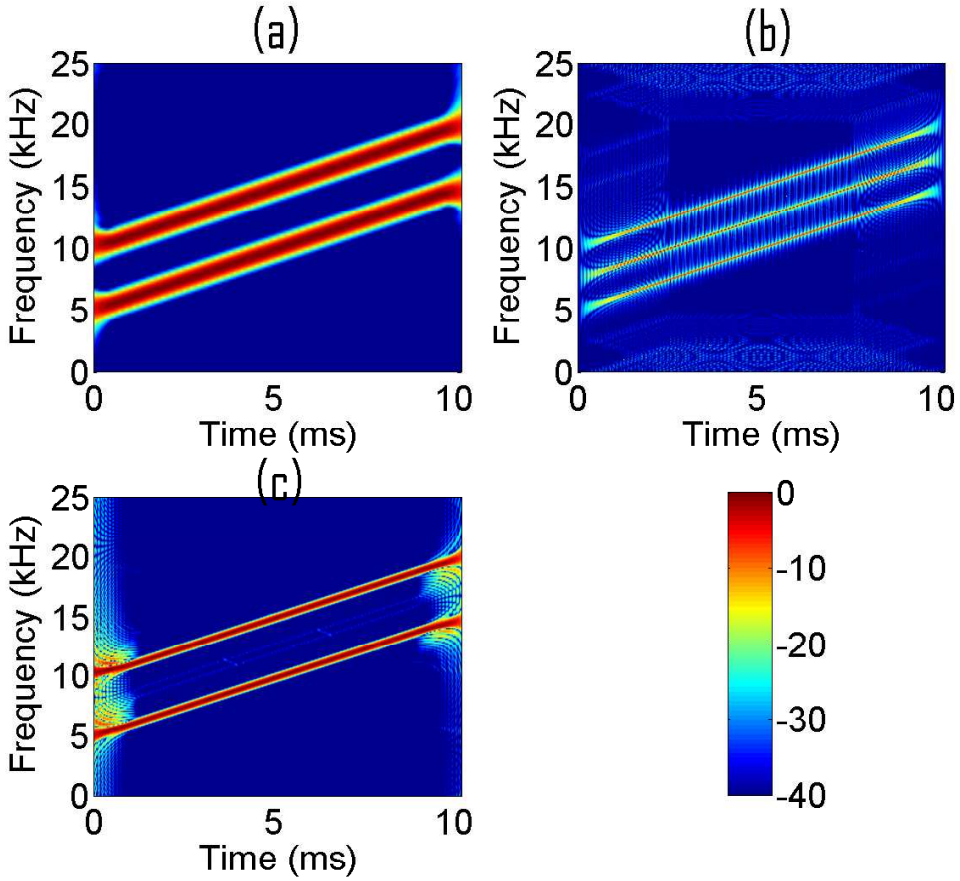

Figure 5: Time-Frequency Representations of signal composed of two linear chirps spanning respectively the frequency bands 5-15kHz and 15-25kHz: (a) is Short Time Fourier Transform (b) Wigner-Ville distribution showing interference patterns between two signals (c) smoothed pseudo Wigner-Ville distribution. The SPWV distribution shows better time and frequency localization then the spectrogram and with reduced interference patterns inherent of the standard Wigner-Ville.

multicomponent signals in the time-frequency plane. More specifically, for a given time-domain signal $s(t)$, the SPWV is defined as:

$$W_s(\tau,\nu) = \int_{-\infty}^{+\infty} h(\tau) \int_{-\infty}^{+\infty} g(u-t)s(u+\frac{\tau}{2})s^*(u-\frac{\tau}{2})\boldsymbol{du}(e^{-j2\pi\nu\tau})\boldsymbol{d\tau} \qquad (14)$$

Where the functions h and g are used to smooth, respectively in the time domain or frequency domain, the kernel of the Wigner-Ville transform $s(u+\frac{\tau}{2})s^*(u-\frac{\tau}{2})$ (i.e. the autocorrelation of the analyzed signal $s(t)$). Hence, contrary to the STFT, the

SPWV transform allows relatively high temporal localization in addition to maintaining frequency resolution. Then by selecting appropriate smoothing functions h and g (e.g. using Hanning window of various lengths) one can minimize the artifacts of interference patterns inherent to the Wigner-Ville transform [3]. The result is a better time-frequency localization then STFT without the complications of interference patterns inherent to standard Wigner-Ville transform (see Fig. 5).

2.3.1 Smoothing Window Selection

Stated previously, the benefit of using the SPWV analysis is the ability to select the time and frequency smoothing windows separately. This does present additional complexity in choosing the appropriate type and size of the window for optimal time and frequency localization. In order to select the window size, further study was conducted on a representative temporal response for a spherical shell computed from Eq. (9). This was selected to investigate the appropriate amount of smoothing for the best visualization of the time-frequency distribution of the echoes of a shell.

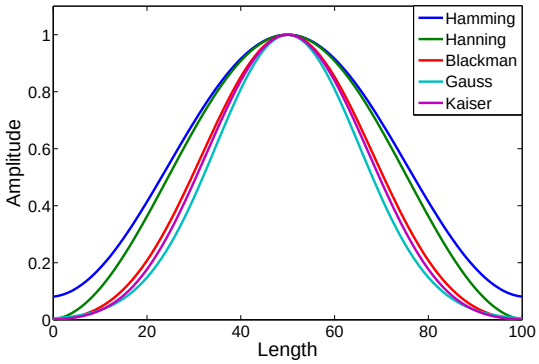

Figure 6: Overlay of standard amplitude smoothing windows including Hanning, Hamming, Blackman, Gauss, and Kaiser. Each window has length of 100 points, and the defining parameters of the Gaussian window and the Kaiser window were selected to be $\alpha = 0.005$, and $\beta = 3\pi$ respectively.

The initial step for selecting a window size was to choose the shape of smoothing window. For this, five types of standard smoothing windows were overlaid to compare

the shape of each windowing function (see Fig. 6). From this plot, it was decided that the Hanning type of window was a good compromise between the sharpness of the Kaiser window, and the broadness of the Hamming window.

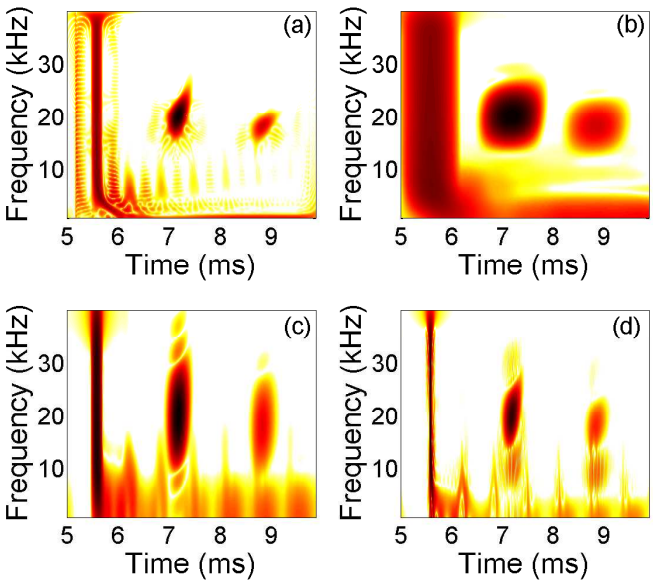

Figure 7: SPWV with different Hanning window sizes with double (wide) and half (narrow) the length of reference smoothing window (reference window sizes are 205 points in time and 171 points in frequency) (a) Narrow window in frequency domain (b) Narrow window in Time domain (c) Broad window in frequency domain (d) Broad window in time domain.

Once the type of window was selected, an empirical study was conducted to evaluate the effect of broad vs. narrow smoothing windows in both time and frequency for the given SPWV representation. These results are shown in Fig. 7. As shown, when little smoothing is used, the results revert to a standard Wigner-Ville distribution in which the interference patterns are prevalent. The goal of getting the smoothing windows set at a desired width in time domain is a balance between suppressing the interference patterns and retaining a good time-frequency localization of a signal. For the given response of the shell, the time smoothing window was determined to be a Hanning window of 0.2ms (205 points) and a frequency smoothing window was a Hanning window of 192Hz (171 points). This is not to say that these are the resolution

limits (which are 0.0012ms and 210Hz), but rather the length of smoothing window. The results of appropriately selected smoothing windows for the SPWV representation are shown in Fig. 8. Though this empirical method is not readily applied in the field, one can select smoothing windows a priori that are appropriate for the targets, and noise anticipated for a given environment.

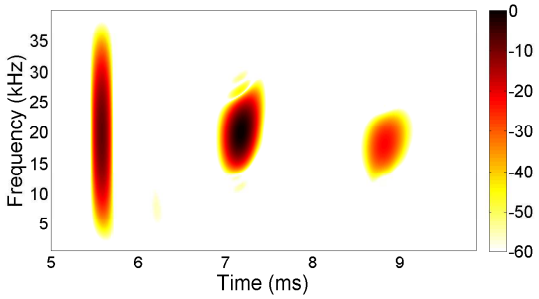

Figure 8: SPWV representation of shell response with appropriate smoothing window size based on empirical study. The Hanning windows used for smoothing were a time window of 0.2ms (205 points) in length and a frequency smoothing window of 192 Hz (171 points).

CHAPTER III

MID-FREQUENCY ENHANCEMENT AND BISTATIC EFFECTS

3.1 Mid-frequency Enhancement

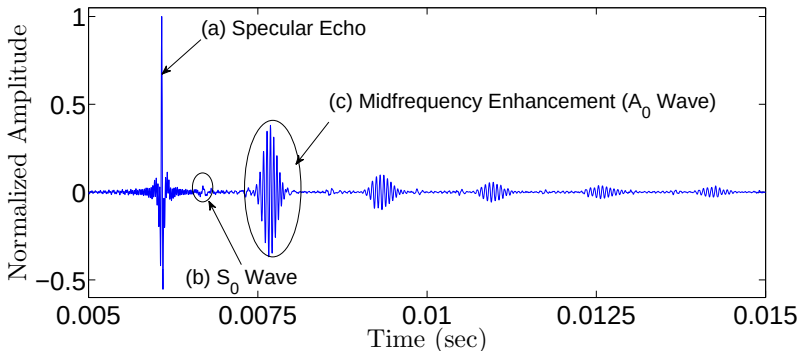

Figure 9: Impulse response of the spherical shell in the backscatter direction $\theta = 180°$ (computed from Eq. (10)) in the frequency band [1Hz-80kHz] using the physical parameters listed in Table 1. The displayed values were normalized by the maximum value of the specular echo. The three arrows indicate the specular echo -labeled (a)- and the echoes of the circumnavigating surface guided waves associated with the first symmetric modes (S_0, -labeled (b)-) and first antisymmetric mode (A_0, labeled (c)) which corresponds to the MFE. Subsequent arrivals correspond to surface guided waves undergoing multiple revolutions around the spherical shell.

Utilizing the modal expansion approach to calculate the full field response from a spherical shell allowed the pressure time series to be calculated for any given (r, θ). Where θ is simply the angle between the direction of the incoming plane wave and the receiver location. Fig. 9 displays the monostatic scattered field (i.e. as recorded by a receiver located at an azimuth $\theta = 180°$ and distance r=10m) computed with the acoustic model described in a previous section (see Fig. 2 and Eq. (10)) using the physical parameters listed in Table 1. A series of narrowband energetic arrivals are clearly visible following the first broadband specular arrival labeled (a) on Fig. 9.

The following weak arrival, labeled (b) corresponds to the first symmetric mode of the shell S_0. This S_0 arrival will not be the focus of this thesis as it does not radiate sound efficiently from the shell (due to the mismatch of phase velocities between this type of wave and the outer medium), and thus has limited interest for practical MCM applications. On the other hand, the next energetic arrival corresponds to the lowest anti-symmetric mode A_0 circumnavigating the shell, labeled (c). The ensuing weaker arrivals are replicas of this mode, which have made subsequent revolutions of the shell. The first energetic return (occurring after only one revolution of the A_0 mode around the shell, see Fig. 2) is characteristic of the MFE [22, 14]. More specifically, the MFE results from the constructive interference of two types of anti-symmetric A_0 waves, classically referred to as A_{0^+} and A_{0^-} depending whether their energetic contribution is mainly localized within the elastic shell (i.e. shell-borne) or within the surrounding fluid (i.e. fluid-borne) at the shell's surface [14]. These two A_0 waves have opposite nature and thus have different dispersion behavior as a result of this bifurcation [19]. Due to the dispersive behavior, the constructive interference between the A_{0^-} and A_{0^+} only occurs within a narrow frequency band near the coincidence frequency f_c (giving raise to the MFE phenomenon). At the coincidence frequency the strong coupling between the A_{0^+} and A_{0^-} waves results in a high level of energy radiating to the surrounding fluid[23].

Looking at a more complete picture of the shell response requires the use of time-frequency analysis. Fig. 10 shows the time response, the frequency response and the SPWV representation of the signal. First note is that the MFE (located at 7.25ms and 20 KHz) is the most energetic feature in the time frequency plane. From this figure, it is clear that the MFE, occurs at a narrow frequency range, when compared to that of the specular (first arrival). Additionally by only analyzing the frequency response (upper-left of Fig. 10) it can be seen that resonance occurs at the frequencies of the MFE. Analyzing the MFE in the time-frequency domain results in localization

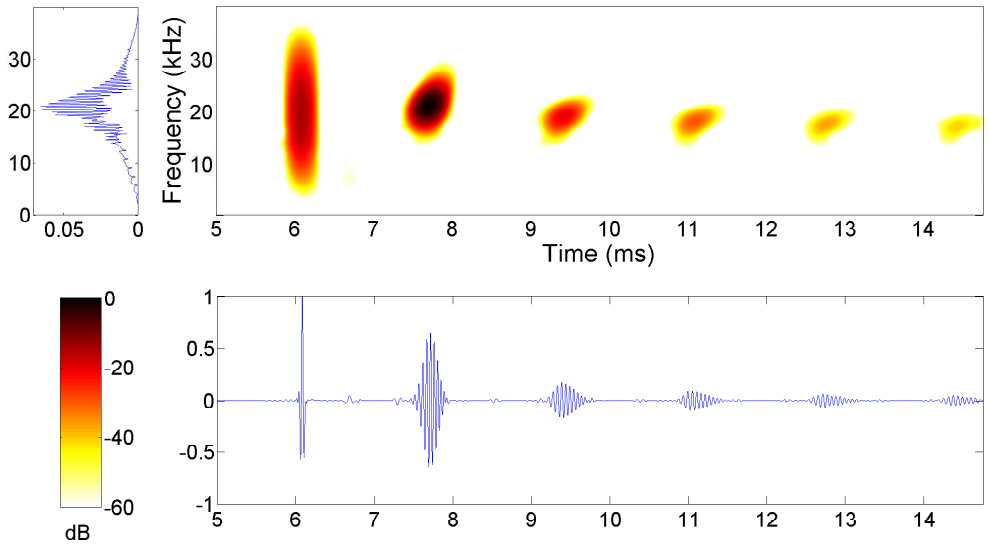

Figure 10: Time-Frequency Representation showing the Fourier representation of the signal in the upper left corner, the time domain response of the signal in the lower right, and the SPWV Time-Frequency representation in the upper right.

information in both time and frequency and is necessary to understand the MFE behavior in the bistatic configurations.

Previous studies for monostatic configurations have shown that the frequency content and repetition rate of these A_0 arrivals (see Fig. 9) contain important information about the shell's geometry (e.g. shell's radius and thickness) and physical properties (e.g. compressional and shear wave velocities in the shell) [13, 24, 11, 31]. It is important to note that the amplitude of the subsequent A_0 arrivals are proportionally reduced by the cumulated radiation damping effects after multiple revolutions around the shell. Hence, these later arrivals are likely to be even more difficult to detect in the presence of high ambient noise or clutter levels. Consequently, the first and most energetic Lamb-wave echo is the most attractive feature for target detection or classification.

3.2 Effect of Environment and Shell Parameters on MFE

Previous work has determined that the center time-frequency peak of the MFE is dependent on the physical properties of the shell; there are additional aspects that affect the time-frequency signature of a given shell [11, 15, 24].

To illustrate the influence of the shell parameters, as well as the outer environmental parameters on the time-frequency content of the MFE, a series of numerical experiments where conducted. To do so the shell's thickness, shell material, and outer medium sound speed were changed to draw basic conclusions about the influence different parameters.

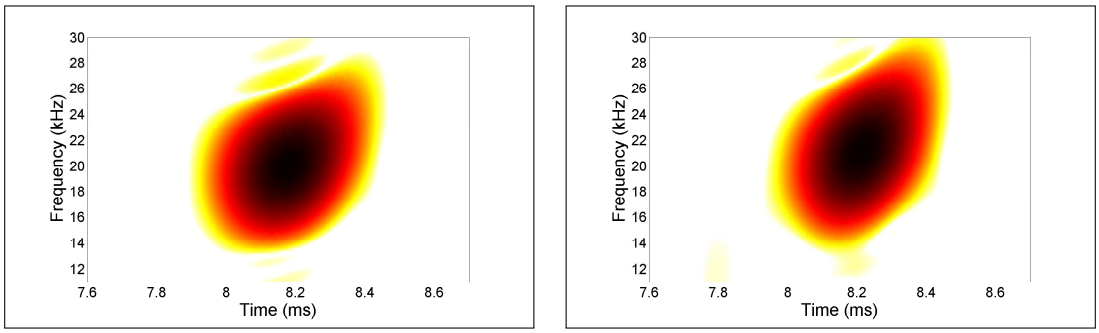

(a) (b)

Figure 11: SPWV representations of the first MFE echo for a spherical shell with two different material types (a) a Steel Shell and (b) same parameters as (a) but with shell made of Titanium.

The result of changing shell material can be seen on close inspection of the MFE in time-frequency plane (see Fig. 11). The center frequency of the MFE remains constant; however, the response in the time-frequency plane changes in shape. Each combination of density, longitudinal and transverse wave speed for a given material results in a unique MFE time-frequency pattern. A change in shell diameter is shown in the difference of arrival time as well as a lower center frequency of the MFE in the reference shell with radius, a=0.53m Fig. 12(a) versus a shell with radius a=0.61m Fig. 12(b). Additionally these experiments further verified that the MFE only occurs

in thin shells. At an outer to inner radius ratio of 0.9, the MFE becomes difficult to detect and with lower ratios (thicker shells) the MFE does not appear to exist. This is as expected due to the nature of Lamb modes whose velocities depend on the relationship between wavelength and plate thickness.

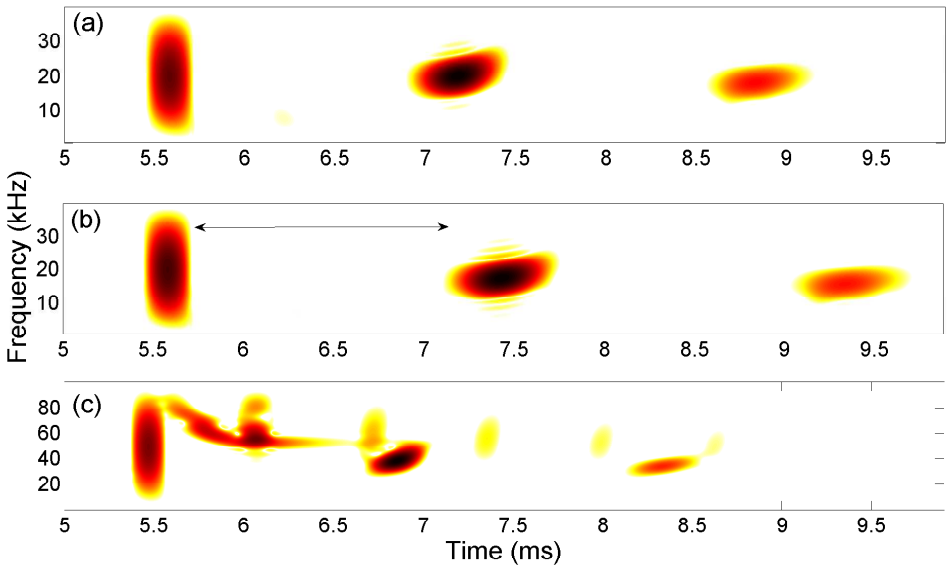

Figure 12: SPWV time-frequency effects on MFE with changing parameters. (a) Reference shell using parameters listed in Table 1. (b) Same as (a) with radius of 0.61m, which lowers the center frequency and increases time between echo repetitions. (c) Same as (a) with a shell surrounded by gravel, which increases the radiated energy from S_0 wave. The parameters used for gravel are $C = 1800m/s$, $C_t = 716m/s$, $\rho = 2000kg/m^3$.

Furthermore, the outer medium effect on the MFE was studied in order to determine the MFE behavior with a change in the type of fluid loading around the shell (see Fig. 12(c)). This can be an important aspect in MCM since objects lying on the bottom of the ocean can become submerged in the sediment. Therefore, the outer medium may change and thus the time-frequency response will differ. Different wave speeds within sediments such as clay or silt not only impact the time-frequency behavior of the MFE but can also increase the energy radiated from of the S_0 waves (due to the change in sound speed and ability for coupling into shear waves) as is

shown in Fig. 12. This increase in radiated energy of the S_0 mode can have a negative impact on the isolation of the MFE echo.

3.3 Time-frequency analysis of the bistatic evolution of spherical shell's scattered field

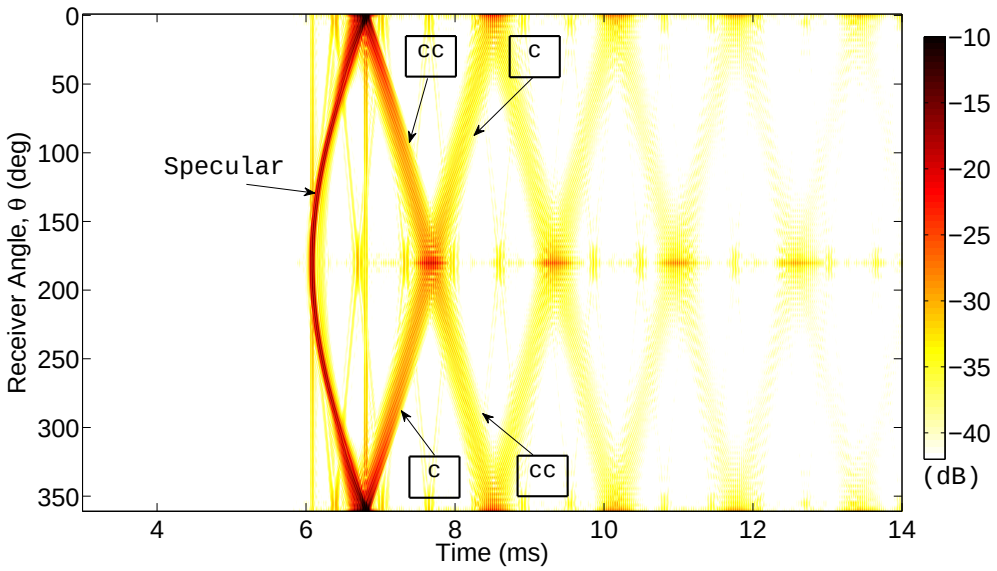

Figure 13: Evolution of the envelope (in logarithmic scale) of the bistatic impulse response of the spherical shell (computed with Eq. (10) using the model parameters listed in Table 1) vs. bistatic angle, θ. The amplitudes were normalized with respect to the maximum values of the scattered field in the monostatic (or backscatter) direction $\theta = 180°$. The first curved arrival corresponds to the specular echo. The two branches of the subsequent X-shaped pattern correspond respectively to the counter-clockwise ("cc" symbol) and clockwise ("c" symbol) propagating components of the A_0 mode. Note that the arrival-times of these two components differ for bistatic receivers (see Fig. 5), except for the monostatic direction $\theta = 180°$ their path around the spherical shell become symmetric with equal lengths.

The behavior of the MFE as a function of time, frequency, and receiver angle is the important aspect to understand in order to process bistatic data efficiently. To determine this behavior in time and angle a traditional plot for radar analysis of a signal was created. As stated previously due to being azimuthally symmetric this problem becomes two dimensional in spherical coordinates (r, θ) and therefore the

focus will be on describing the behavior in relation to the dimensions of importance [4].

Fig. 13 displays the evolution of the envelope of the simulated bistatic responses of the elastic shell, computed using Eq. (10) and the model parameters listed in Table 1, for a full 360° revolution of receiver angle θ. Note, that the values displayed for $\theta = 180°$ correspond to the envelope of the monostatic time series shown in Fig. 9. The first wavefront visible on this time vs. angle representation, with nearly constant amplitude over all receiver angles, corresponds to the broadband specular reflection of the shell recorded in free space. The two branches of the following "X-shaped" pattern (between $6.5ms \leq t \leq 8.5ms$), labeled "c" and "cc" on Fig. 13, correspond, respectively, to the interference of the circumnavigating A_{0^+} and A_{0^-} waves (MFE, see chapter 3.1) radiating sound around shell while propagating, respectively, in the clockwise and counter-clockwise directions. This difference in arrival time between the clockwise and counter-clockwise interference patterns can be simply explained from a geometric ray analysis, as presented in chapter 3.4 (see Fig. 3). Furthermore, as expected, these clockwise and counter-clockwise interference patterns intersect in the monostatic direction $\theta = 180°$ as they both have the same path length around the shell before reaching the receiver. Consequently, the MFE pattern is most energetic in the monostatic configuration where all four A_0 wave components (i.e. both clockwise and counter-clockwise circumnavigating A_{0^+} and A_{0^-} waves) interfere constructively.

As shown quantitatively on Fig. 13, the energetic MFE pattern begins to split into two branches as the receiver moves away from the monostatic configuration ($\theta = 180°$), and the MFE amplitude rapidly decays[9]. Consequently, for practical MCM applications in noisy environments, bistatic measurements of the MFE would likely need to be combined coherently, using some type of array processing, in order to enhance the bistatic detectability of the MFE pattern. However, a coherent combination of these bistatic A_0 wave echoes using standard time-delay beamforming

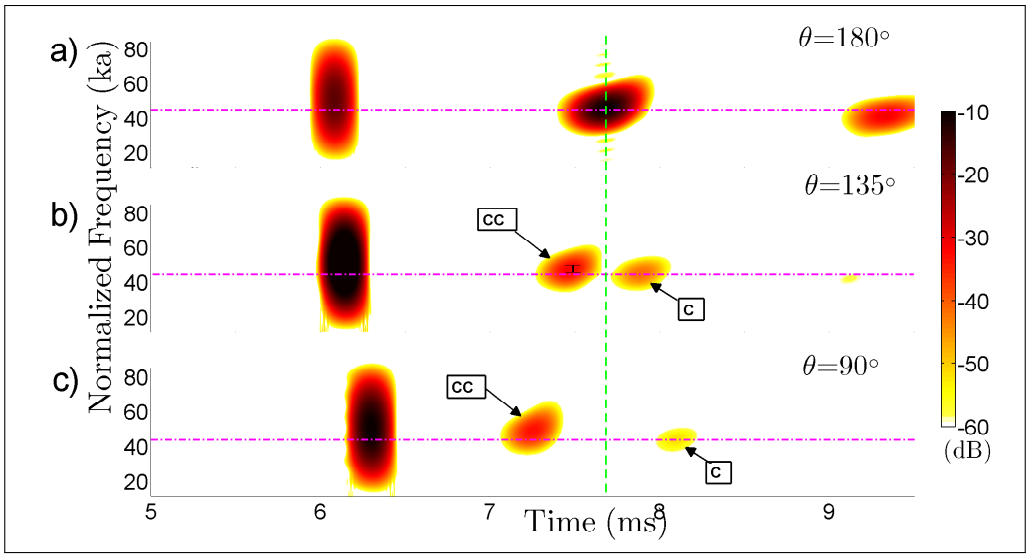

Figure 14: Smoothed Pseudo-Wigner Ville representation (in logarithmic scale) of the impulse response of the spherical shell for three representative receiver's azimuth angles (a) monostatic direction $\theta = 180°$, or bistatic directions (b) $\theta = 135°$ and (c) $\theta = 90°$. The energetic MFE echo (due to the interference of the clockwise and counterclockwise propagating A_0 wave) in the monostatic direction is visible at time $t = 7.66ms$ (dashed vertical line) and a normalized frequency $ka = 46$ (dashed horizontal line). The bistatic configurations illustrate the progressive splitting of the MFE echo into two distinct clockwise and counterclockwise arrivals (see Fig. 3), as well as their relative time-frequency shift with respect to the monostatic echo. For each angle the magnitude were normalized by the maximum displayed value.

(i.e. after compensating for their relative time shift), would not be optimal if the frequency content of the MFE vary with bistatic each receiver angle θ. To test this hypothesis, the SPWV transform, as described in chapter IV (see Eq. (14)), is used hereafter to investigate the time-frequency analysis of the bistatic MFE pattern.

Fig. 14 depicts the SPWV of the time-series computed for three different bistatic angles spaced apart by 45° ($\theta = 180°, 135°, 90°$). The selected smoothing functions for the SPWV analysis were Hanning windows yielding a time and frequency resolution of 2μs and 205Hz (see Eq. (2)). As predicted, the SPWV associated with angles $\theta = 135°$ and $\theta = 90°$ illustrates the splitting of the energetic main MFE pattern's arrival (as shown for $\theta = 180°$, see Fig. 14(a)) into two weaker distinct arrivals with the left (respectively right) pattern corresponding to counter-clockwise (respectively

clockwise) interference pattern, as labeled on Fig. 14(b-c). Less intuitively, this time-frequency analysis reveals also that the counter-clockwise (respectively clockwise) MFE pattern also exhibits an upward (downward) frequency shift (of respectively $+1.8ka$ or $-1.1ka$ for $\theta = 135°$) when compared to the monostatic MFE pattern. A physical interpretation of this time-frequency shift will be presented in the next section using a quantitative ray analysis for spherical shell scattering. Furthermore, as discussed in chapter IV, a generalized time-frequency beamformer can be developed to compensate for the observed time-frequency shifts of the bistatic MFE as revealed by the SPWV analysis. Indeed, similar time-frequency beamformers have previously been developed in order to compensate for wideband Doppler effects when tracking a moving source[27].

3.4 Physical interpretation of the time-frequency evolution of the bistatic MFE pattern from quantitative ray theory

To provide a more intuitive understanding of the behavior of the MFE in various source and receiver orientations, the use of an approximate ray theory will be used. The ray theory presented in chapter 2 will be used to understand the expected time and frequency behavior of the MFE, and therefore allow time and frequency compensation to be made when combining the MFE measured at various bistatic angles.

In the vicinity of the coincidence frequency, the phase velocity of the A_{0^-} becomes close to the value of the sound velocity of the surrounding fluid C_0 (see Fig. 4(a)). Consequently, the angle of incidence becomes $\alpha \approx \pi/2$ based on Eq. (11), which simplifies the computation of the path length of the A_{0^-} wave propagating around the shell (see Fig. 3). For a bistatic receiver, the arc path angles ϕ_c and ϕ_{cc} of respectively the clockwise (see Fig. 3(a)) and the counter-clockwise (see Fig. 3(b)) propagating A_{0^-} waves differ such that:

$$\phi_{cc}(\theta) = \frac{\pi}{2} + \theta - cos^{-1}\left(\frac{a}{r}\right) \tag{15}$$

$$\phi_{c}(\theta) = \frac{5\pi}{2} - \theta - cos^{-1}\left(\frac{a}{r}\right) \tag{16}$$

Where θ is the bistatic receiver angle, a is the shell's outer radius and r is the distance between the sphere's centroid and the receiver distance (r). Note that $\phi_c = \phi_{cc}$ only when $\theta = \pi$ (i.e. for a monostatic configuration)

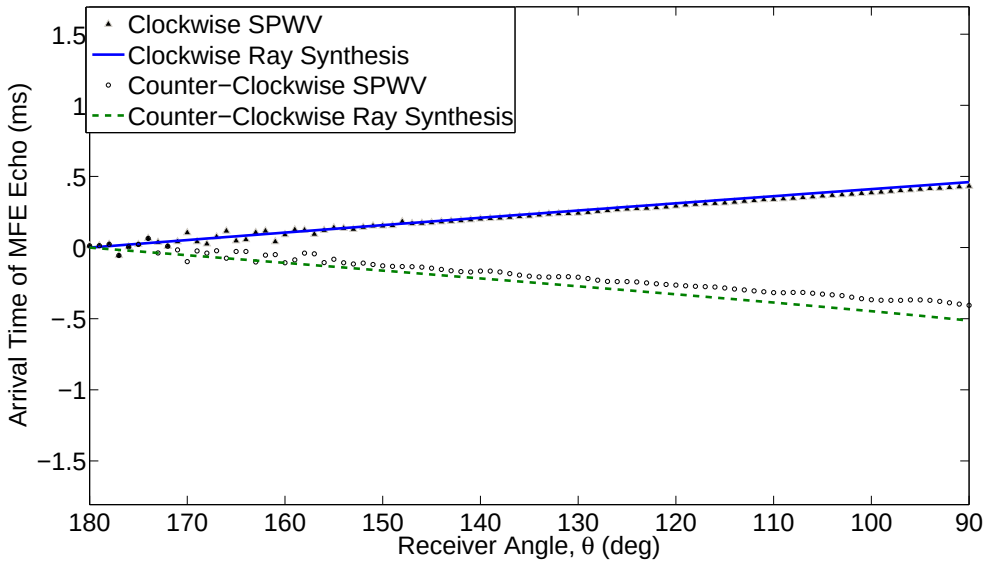

Figure 15: Variations of the arrival time of the MFE echo vs. bistatic receiver angle θ (see geometry in Fig. 3) with respect to the monostatic arrival time of the MFE (i.e. $\theta = 180°$). The triangle and circle symbols indicate the measured arrival times for respectively the clockwise and counter-clockwise A_{0^-} waves, as measured using the local maxima in the time-frequency plane of the smoothed pseudo Wigner-Ville representation of the bistatic scattered field (see Fig. 14). For comparison, the solid and dashed lines correspond to the arrival-times predicted from the ray synthesis for the same clockwise and counter-clockwise A_{0^-} waves.

Overall, the difference in path length between the clockwise and the counter-clockwise propagating A_{0^-} waves determines the apparent time-frequency shift of the bistatic MFE arrival as measured by the SPWV analysis (see Fig. 14). More specifically, the local maximum of the SPWV amplitude in the time-frequency plane

indicates the arrival time of the propagating energy of the A_{0^-} wave packet, and is thus determined by the value of the group velocity, $C_{group}(ka = 46)$, A_{0^-} wave in the vicinity of the coincidence frequency (ka=46 see Fig. 4(b))[29]. Hence for a bistatic angle θ the variations of the arrival-time for the clockwise and the counter-clockwise propagating A_{0^-} waves (with respect to the arrival times in the monostatic configuration i.e. $\theta = \pi$) can be simply predicted from the ray analysis. This is done using the following expressions $(\pi - \theta)a/C_{group}(ka = 46)$ and $-(\pi - \theta)a/C_{group}(ka = 46)$ (for $90° \leq \theta \leq 180°$). Fig. 15 shows a good agreement between these linear predictions of the time-shift of the MFE arrival from the ray analysis (plain and dashed lines) and the measured values from the SPWV analysis (dotted lines) for bistatic angles varying between $\theta = 90° \leq \theta \leq 180°$. The slight discrepancy visible around 90° between the measured and predicted arrival times for the counter-clockwise wave (dashed line) likely result from error in arrival-time selection from the SPWV due to interferences occurring between the S_0 arrival and the A_{0^-} arrival.

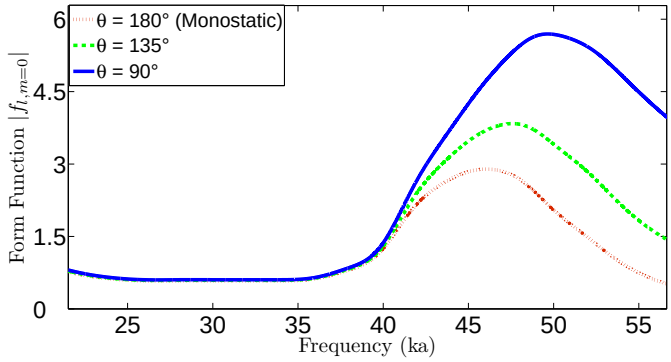

Figure 16: Ray models of the amplitudes of the earliest counter-clockwise A_{0^-} wave arrival (based on the form function, $f_{l,m}$ given by Eq. (13) for $m = 0$) in the vicinity of the coincidence frequency for same three bistatic receiver angles θ shown in Fig. 14. Note the maximum of the amplitude's enhancement in the mid-frequency region progressively increases from $ka \approx 46$ at $\theta = 180°$ to $ka \approx 49$ at $\theta = 90°$.

The quantitative ray analysis can also be used to predict the apparent frequency shift of the bistatic MFE arrival (see Fig. 14). More specifically, as the bistatic angle

θ varies away from π, the arc path angles ϕ_c and ϕ_{cc} (see Eq. (15-16)) of respectively the clockwise and the counter-clockwise propagating A_{0^-} waves vary as stated earlier (see Fig. 3). Consequently, for a given bistatic angle θ, the MFE occurs at the normalized frequency ka which maximizes the form function associated with the ray corresponding to the first A_{0^-} arrival, i.e. $|f_{l=A_{0^-},m=0}(\phi)| = |B_l\beta_l(ka)e^{(-\phi(\theta)\beta_l(ka))}|$, for $\phi = \phi_{cc}$ or $\phi = \phi_c$ (see Eq. (15-16)). Hence the frequency dependence of the radiation damping parameter $\beta_l(ka)$ (see Fig. 4(c)) ultimately determines the apparent frequency shift of the bistatic MFE arrival. As an illustration of this phenomenon, Fig. 16 displays the evolution of magnitude of the form function $|f_{l=A_{0^-},m=0}(\phi)|$ for the counter-clockwise propagating A_{0^-} wave for the same three bistatic angles ($\theta = 180°, 135°, 90°$) used for the SPWV calculations shown in Fig. 14.

As the bistatic angle θ decreases from $\theta = 180°$ to $\theta = 90°$, it can be observed that the maximum of the form function shifts upward towards higher normalized frequency values from $ka = 46$ to $ka = 49$ (i.e. in the vicinity of the coincidence frequency) for the counter-clockwise propagating A_{0^-} wave. A similar analysis can be conducted to quantify the downward frequency shift of the clockwise propagating A_{0^-} wave. Overall, Fig. 17 shows a good agreement between the bistatic frequency shifts predicted by this quantitative ray analysis and the frequency-shifts values measured from the SPWV analysis (dot symbols) of the computer time-series. There is however a slight bias between the predicted frequency and the measured frequency, which is caused by the difference in measuring the peak of the signal amplitude versus the peak of the energy envelope. Furthermore, the spread of the frequency-shift measurements falls within the measurement error of the SPWV analysis, which is determined by the frequency resolution of the smoothing kernel (indicated by the vertical error bar displayed on Fig. 17). This measurement error can potentially be mitigated by reducing the frequency smoothing of the SPWV. However doing so could increase the interference pattern artifacts of the Wigner-Ville analysis, which would in turn bias

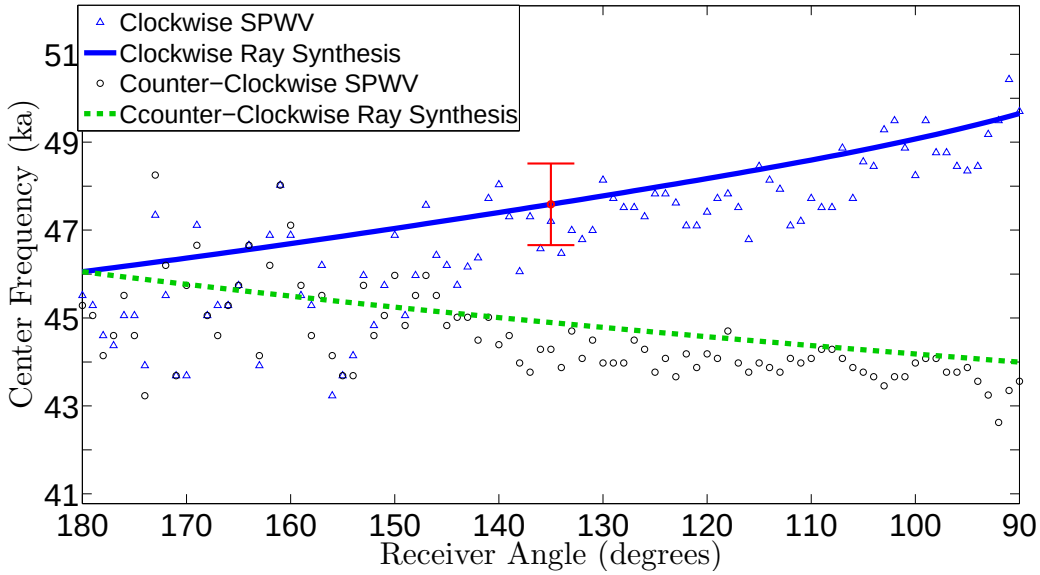

Figure 17: Variations of the normalized center frequency of the MFE echo (i.e. coincidence frequency) vs. bistatic receiver angle θ (see geometry in Fig. 1) with respect to the monostatic arrival time of the MFE (i.e. $\theta = 180°$). The triangle and circle symbols indicate the center frequencies for respectively the clockwise and counter-clockwise A_0 arrival as measured from the local maxima in the time-frequency plane of the smoothed pseudo Wigner-Ville (SPWV) representation of the bistatic scattered field (see Fig. 3). The vertical error bar depicts the measurement resolution along the frequency axis on the SPWV representation, which accounts for most of the spread in the measured values. For comparison, the solid and dashed lines correspond to the center frequency of MFE echo predicted from the theoretical ray amplitude variations as shown on Fig. 16.

the estimation of the SPWV maxima in the time-frequency plane [3].

CHAPTER IV

APPLICATION TO TIME-FREQUENCY BEAMFORMING

The time vs. angle representation displayed in Fig. 13 shows that the MFE persists for bistatic source-receiver configurations, and thus still carries information about the physical features of the elastic shell. However, the bistatic amplitude of the A_0 wave arrival is significantly reduced compared to the monostatic configuration. Consequently, bistatic detection of thin spherical shells could potentially be challenging in the presence of high clutter or high ambient noise levels. Therefore, bistatic detection of the MFE would need to be enhanced for practical implementations, by coherently combining the signals measured on an array of receivers using beamforming techniques [26]. To do so, it is necessary to use a generalized time-frequency beamformer to account for the time-frequency shifts occurring between the various bistatic A_0 wave echoes recorded on an array of sensors surrounding the spherical shell. This generalized time-frequency beamformer can be implemented using a similar formalism developed when compensating for wideband Doppler effects when tracking a fast moving acoustic source based on companded (or time-scaled) replica of the Doppler-free source signal [27]. The term "companded" is a portmanteau of *comp*ressed and ex*panded*. It is assumed hereafter that the bistatic A_{0^-} arrival recorded at a bistatic angle θ_j is centered at time t_j and frequency f_j in the time-frequency plane. Additionally, the scattered time-domain signal recorded by the j^{th} receiver located at a bistatic angle θ_j is noted $P_j(t)$ $(j = 1..N)$. A generalized time-frequency beamformer $B(t; N)$ can then be defined by combining companded versions of the N receiver signals $P_j(t)$

such that:

$$B(t;N) = \sum_{j=0}^{N} P_j(\gamma_j(t+\tau_j)) \tag{17}$$

where the parameter $\tau_j = t_j - t_1$ is selected to compensate the apparent bistatic time-shift (e.g. see Fig. 7) of the A_{0^-} wave, defined here with respect to the bistatic arrival time of the A_{0^-} wave recorded on the first receiver. Similarly, the companding (or time-scaling) parameter $\gamma_j = 1 + (f_j - f_1)/f_1$ is selected to compensate for the apparent bistatic frequency-shift the A_{0^-} wave (e.g. see Fig. 9). The values of the parameters τ_j and γ_j can be estimated based on predictions from the quantitative ray analysis (as described in chapter 3.4) or by directly measuring the time-frequency shifts of the bistatic A_{0^-} arrival from SPWV analysis (as described in chapter 3.3), the later being the selected approach hereafter. It can be noted that when $\gamma_j = 1$ (i.e. in the absence of frequency-shift), the expression of the generalized time-frequency beamformer shown in Eq. (17) reduces to the expression of the conventional time-delay beamformer [26, 27].

As an illustration of the proposed array beamforming methodology, the upper panel of Fig. 18(a) displays the A_{0^-} arrivals recorded by five bistatic sensors uniformly distributed in azimuth around the spherical shell between $100^\circ \leq \theta \leq 140^\circ$. The analysis window was limited to the first A_{0^-} echo. These A_{0^-} arrivals were simply time-aligned with respect to the counter-clockwise MFE arrival for the first receiver (j=1, $\theta_1 = 100^\circ$). It can be noted that the shape of the waveforms remain slightly different due to the bistatic frequency-shift of the A_{0^-} wave (see chapter 3.3 and 3.4). Additionally, the maximum amplitude of each receiver signal $P_j(t)$ was normalized to unity, to account for the bistatic amplitude variations of the A_{0^-} arrival (see Fig. 3) so that each receiver had an equal contribution to the beamforming summation in Eq. (17). These five time-aligned and normalized waveforms were then simply summed to generate the output of the conventional time-delay beamformer (i.e. using Eq. (17) with N=5 and $\gamma_j = 1$), as shown on the lower panel of Fig. 18(a). The maximum of

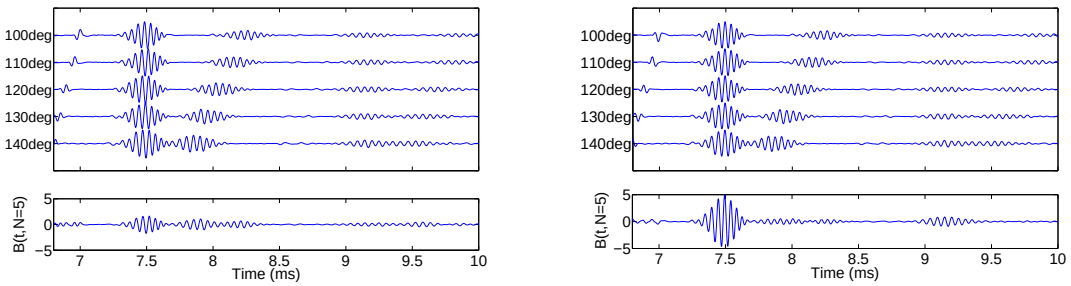

Figure 18: (a) Upper Panel: Stacked representation of the time-aligned arrivals of counter-clockwise propagating A_{0^-} waves (see Fig. 13) recorded at five different bistatic angles. The relative bistatic time-shifts, with respect to first bistatic angle $\theta_1 = 100^\circ$ were obtained from the SPWV analysis (see Fig. 15). Lower Panel: Coherent addition of the five time-shifted waveforms using a conventional time-delay beamformer (computed by when setting the companding parameter as $\gamma_j = 1$- see Eq. (17)). (b) Upper Panel: same as (a), but each waveform was also companded to account for the apparent frequency shift of the bistatic counter-clockwise propagating A_{0^-} arrival-with respect to the first bistatic angle $\theta = 100^\circ$- based on the measured frequency-shifts values from the SPWV analysis (see Fig. 17). Lower Panel: Coherent addition of the five time-frequency shifted waveforms using a generalized time-frequency beamformer (see Eq. (17)). Note that each bistatic waveform, in both upper panels, was normalized to its maximum value, such that one would expect a maximum beamformer output of 5 when an optimal coherent addition is achieved.

.

this conventional time-delay beamformer signal is only 1.63 (i.e. < 5) which indicates that the five received signals were not coherently added in an optimal fashion. On the other hand, the upper panel in Fig. 18(b) displays the A_{0^-} arrival for the same five receivers, but after applying both time shift and frequency shift corrections to each waveform based on the measured values from respectively Fig. 15 and Fig. 17 for the counter-clockwise A_{0^-} echo. The lower panel of Fig. 18(b) shows that the maximum of the generalized time-frequency beamformer, computed using Eq. (17), is equal to 4.98 and thus close to the optimal value of 5. Hence, this value indicates that the five received signals were indeed added coherently in a near optimal fashion using the generalized time-frequency beamformer (see Eq. (17)).

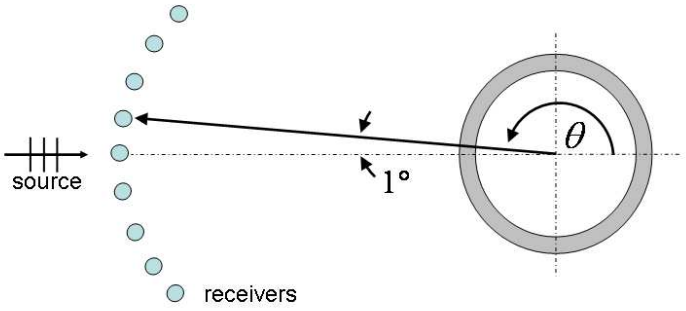

Figure 19: Schematic of the bistatic receivers layout around the spherical shell used for the numerical simulations (see Fig. 20). Each receiver array is centered on the monostatic direction-$\theta = 180°$-and is composed of an odd number N of receivers which are uniformly spaced in azimuth angle at 1° apart.

The influence of the receiver arrays aperture (i.e. the number N of bistatic receivers) on the performance of the generalized time-frequency beamformer (see Eq. (17)) is investigated next. Fig. 19 displays the layout of the bistatic receivers around the spherical shell which are centered on the monostatic direction $\theta = 180°$. These receivers are uniformly spaced in azimuth angle at 1° apart which implies a relative shift of the center frequency of the counter-clockwise A_{0^-} echo of approximately $250Hz$ between two consecutive receivers based on the results displayed in Fig. 9. Fig. 20 displays the variations of the maximum value of the generalized time-frequency beamformer $B(t;N)$ (dot symbols) for an increasing number of receivers N (i.e. corresponding to an increasing azimuthal aperture of the receiver array). Similarly, to the results shown in Fig. 18(b), each counter-clockwise A_{0^-} arrival was also companded to account for the apparent frequency shift between bistatic receivers. As expected, the maximum value of the generalized time-frequency beamformer $B(t;N)$ linearly increases with the number of receivers (up to $N = 19$ here), thus indicating that all counter-clockwise A_{0^-} arrivals were indeed coherently process across the array aperture. For comparison the maximum value of the conventional time-delay beamformer

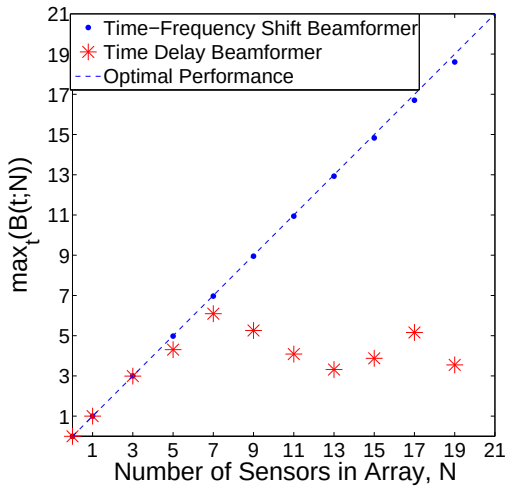

Figure 20: Evolution of the maximum value of the array beamformer $B(t;N)$ (see Eq. (17)) for increasing number of receiver N (equivalent here to an increasing angular aperture of the receiver array see Fig. 19). Asterisk and dot symbols mark respectively the values obtained the conventional time-delay beamformer formulation (i.e. when the companding (or time-scaling) parameter is set to $\gamma_j = 1$) or the generalized time-frequency beamformer formulation. The linear dependency of the number of N of receiver (dashed line) is also added for comparison and corresponds to the optimal achievable value of the array beamformer output $B(t;N)$ when the arrivals of counter-clockwise propagating A_{0^-} waves recorded by the N receivers add in phase coherently.

(star symbols) are also displayed on Fig. 20. It can be observed that those values start to significantly deviate from the optimal linear increase beyond $N = 5$ receivers. These numerical results thus confirm that conventional time-delay beamformer would not be an optimal way to coherently processed MFE arrivals recorded across a bistatic aperture.

CHAPTER V

CONCLUSIONS

The bistatic acoustic scattering of a fluid-loaded spherical elastic shell was investigated both numerically, using a partial wave series expansion, and theoretically using a quantitative ray analysis. This study focused on the most energetic bistatic echoes (also referred to as mid-frequency enhancement echo, or MFE) which are associated with the circumnavigating first antisymmetric guided wave (primarily its A_{0^-} modal component). In particular, the time-frequency analysis of the MFE was conducted using the Wigner-Ville transform.

The following three conclusions can be drawn from this investigation. First, as revealed from the Wigner-Ville analysis, the bistatic MFE echoes exhibit a time-shift and frequency-shift, as well as a decrease in amplitude, with respect to the monostatic receiver configuration. Second, a simple quantitative ray theory can be used to predict these observed time-frequency shifts of the MFE arrival, which primarily results from the combined effect of 1) the bistatic variations of the path length around the spherical shell of the clockwise or counter-clockwise circumnavigating A_{0^-} waves, and 2) the frequency dependence of the radiation damping parameter for the A_{0^-} wave. Finally, from an operational point of view, a generalized time-frequency beamformer can be used for coherently processing the bistatic MFE echoes recorded along a distributed receiver array around the spherical shell. This generalized time-frequency beamformer uses companded replica of the bistatic MFE echoes to account for the relative time-frequency shift of the MFE arrival between receivers.

Overall, the results of this study demonstrated that time-frequency variations of the bistatic echoes associated with the structural response of elastic spherical shell

could be predicted. Additionally, due to the apparent bistatic time-frequency shifts of these MFE echoes, optimal coherent processing of those weak MFE echoes cannot be achieved by conventional array processing techniques simply relying on variants of the time-delay beamformer algorithm. In particular, these results imply that conventional Synthetic Aperture Sonar (SAS) algorithms may not yield optimal imaging results for the detection and classification of the MFE echoes of spherical elastic shells insonified by low-frequency bistatic sonar systems. Similar conclusions may be applicable to elastic shells with other canonical shapes supporting propagating guided waves (such as finite cylinders). Further joint theoretical and numerical analysis, as well as at-sea experiments, are required to understand the mechanisms of bistatic echo formation for elastic shells and the time-frequency coherence of structure-borne acoustic echoes. Such studies should provide valuable insights to guide the design of optimal receiver architecture for low-frequency bistatic sonar systems (e.g. using distributed sensor networks) and SAS imaging algorithms.

APPENDIX A

MATLAB CODE

```
%       Acoustic Scattering by a Spherical Shell
global file
%file =['nswc1.txt'];
%file =['exp1.txt'];
%file =['goats98_shell.txt'];
file =['marston_shell.txt'];
clc;
disp(['Experiment File: ',file]);
readfile;    %Read Parameters file.
sweep_theta=[90:1:270];
sweep_dist=[10];
%%
%-----------    First and Second Lame Coefficient         ----------------%
% Observation medium ("OUTSIDE")
  mu1 =    rho1*ct1^2;
  lamda1 = rho1*cl1^2-2*mu1;

% SHELL
  mu2    =    rho2*ct2^2;
  lamda2 = rho2*cl2^2-2*mu2;
%-------------------------------------------------------------------------%
jkr=[];ykr=[];
%phi1=[];
reduced_freq=[];
ent=0;
```

```
cnt_freq=0;
for f=fmin:df:fmax
    %clc;disp(['Estimated % Completed: ',num2str(f/fmax*100,3),' %']);
    cnt_freq=cnt_freq+1;
  omega =  2*pi*f;           % pulsation
  K     =  omega/cl1;        %WAVENUMBER in SURROUNDING medium.vecteur
                             %   d'onde dans le milieu d'bservation
  Kl    =  omega/cl2;        %Longitudinal WAVENUMBER in the shell
  Kt    =  omega/ct2;        %Transverse WAVENUMBER in the shell
  X     =  K*a;              %Reduced frequency. Surrounding medium,
  Xl    =  Kl*a;             %Longitudinal Reduced frequency. Shell.
  Xt    =  Kt*a;             %Transverse Reduced frequency. Shell.
  Y     =  omega/cl3*b;     % WAVENUMBER MEDIUM (III) INSIDE the shell
  Yl    =  Kl*b;
  Yt    =  Kt*b;
  reduced_freq=[reduced_freq X];

  ord = (0:1:nb_mode)';

%   Bessel Function. Also First and Second derivative :

    [jX,yX,jpX,ypX,jsX,ysX ]      = bes_prim_sec_hs(ord,X) ;
    [jXl,yXl,jpXl,ypXl,jsXl,ysXl ]= bes_prim_sec_hs(ord,Xl);
    [jXt,yXt,jpXt,ypXt,jsXt,ysXt ]= bes_prim_sec_hs(ord,Xt);
    [jY,yY,jpY,ypY,jsY,ysY ]      = bes_prim_sec_hs(ord,Y) ;
    [jYl,yYl,jpYl,ypYl,jsYl,ysYl ]= bes_prim_sec_hs(ord,Yl);
    [jYt,yYt,jpYt,ypYt,jsYt,ysYt ]= bes_prim_sec_hs(ord,Yt);
    cnt_r=0;
    for dist_r=sweep_dist
        cnt_r=cnt_r+1;
        [jkr(:,cnt_freq,cnt_r),ykr(:,cnt_freq,cnt_r),...
            jpkr,ypkr,jskr,yskr ]= bes_prim_sec_hs(ord,(K*dist_r)) ;
```

```
    end

% Hankel Functions.

    h1X  = jX  + i*yX  ;
    h1pX = jpX + i*ypX ;
    h1sx = jsX + i*ysX ;

%----------------DETERMINANT PARAMETES-----------------------------------

  a11 = rho1/rho2*h1X;
  a12 = (lamda2*jXl-2*mu2*jsXl)/(lamda2+2*mu2) ;
  a13 =  -2*ord.*(ord+1).*(Xt*jpXt-jXt)/Xt^2;
  a14 = (lamda2*yXl-2*mu2*ysXl)/(lamda2+2*mu2);
  a15 =  -2*ord.*(ord+1).*(Xt*ypXt-yXt)/Xt^2;
  %a16 =0;

  a21 = X*h1pX;
  a22 = Xl*jpXl;
  a23 = ord.*(ord+1).*jXt;
  a24 = Xl*ypXl;
  a25 = ord.*(ord+1).*yXt;
  %a26 = 0;

  %a31 = 0;
  a32 = 2*(Xl*jpXl-jXl);
  a33 =  (ord+2).*(ord-1).*jXt+Xt^2*jsXt;
  a34 = 2*(Xl*ypXl-yXl);
  a35 =(ord+2).*(ord-1).*yXt+Xt^2*ysXt;
  a36 =zeros(nb_mode,1);

  %a41 = 0;
```

```
  a42 = (lamda2*jYl-2*mu2*jsYl)/(lamda2+2*mu2);
  a43 =  -2*ord.*(ord+1).*(Yt*jpYt-jYt)/Yt^2;
  a44 = (lamda2*yYl-2*mu2*ysYl)/(lamda2+2*mu2);
  a45 = -2*ord.*(ord+1).*(Yt*ypYt-yYt)/Yt^2;
  a46 = jY*rho3/rho2;

  %a51 =0;
  a52 = Yl*jpYl;
  a53 = ord.*(ord+1).*jYt;
  a54 = Yl*ypYl;
  a55 = ord.*(ord+1).*yYt;
  a56 = Y*jpY;

  %a61 =0;
  a62 = 2*(Yl*jpYl-jYl);
  a63 = (ord+2).*(ord-1).*jYt+Yt^2*jsYt;
  a64 = 2*(Yl*ypYl-yYl);
  a65 = (ord+2).*(ord-1).*yYt+Yt^2*ysYt;
  %a66 = 0;

  a1 =jX*rho1/rho2;
  a2 =X*jpX;

  %%Expression of the scalar potential (phi1) associated with the scattered
  %%pressure field by the spherical shell.
Al1=[];
%Pl_theta=genpol(nb_mode,cos(theta_rd))';%%Create Legendre Polynomial
    for l=1:nb_mode+1
        if l==1
            dl=[ a11(l) a12(l)  a14(l)    0    ; ...
                 a21(l) a22(l)  a24(l)    0    ; ...
                  0     a42(l)  a44(l)  a46(l) ; ...
```

```
                0     a52(l)  a54(l)  a56(l)];
        else
              dl= [ a11(l) a12(l) a13(l) a14(l) a15(l)   0   ; ...
                    a21(l) a22(l) a23(l) a24(l) a25(l)   0   ; ...
                     0     a32(l) a33(l) a34(l) a35(l)   0   ; ...
                     0     a42(l) a43(l) a44(l) a45(l) a46(l); ...
                     0     a52(l) a53(l) a54(l) a55(l) a56(l); ...
                     0     a62(l) a63(l) a64(l) a65(l)   0  ];
        end

         aux=dl;
         aux(1,1)=a1(l);
         aux(2,1)=a2(l);
         dl1=aux;
         Al1=[Al1;(- i^l*(2*l+1)*det(dl1)/det(dl))];
    end
    Al2(:,cnt_freq)=Al1;
end
Pole=sum(Al1);
%

clear Al1 dl1 aux dl a2 a1 a65 a64 a63 a62 a56 a55 a54 a53 a52 a46 a45 a44 a43 a42 a3
    a33 a32 a25 a25 a24 a23 a22 a21 a15 a14 a13 a12 a11 h1sx h1X jX yX jpX ypX jsX ys
    ysXl jXt yXt jpXt ypXt jsXt ysXt jY yY jpY ypY jsY ysY jYl yYl jpYl ypYl jsYl ysY
    ysYt jpkr ypkr jskr yskr frequency dist theta K Kl Kt X Xl Xt Y Yl Yt...
    alpha0_rd b cl1 cl2 cl3 ct1 ct2 ct3 ent f h1pX l lamda1 lamda2 mu1 mu2 omega ord
    reduced_freq rho1 rho2 rho3 s z;

phi_all=zeros(length(sweep_theta),(fmax/df),length(sweep_dist));
cnt_theta=0;
%phi1=zeros(1,cnt_freq);
for theta=sweep_theta
```

```
    cnt_theta=cnt_theta + 1;
    theta_rd=theta*pi/180;
    Pl_theta=genpol(nb_mode,cos(theta_rd))';%%Create Legendre Polynomial
    for dist=1:cnt_r
       for frequency=1:cnt_freq
        phi1l=nansum(Pl_theta.*Al2(:,frequency).*(jkr(:,frequency,dist)+...
            i*ykr(:,frequency,dist))); % Modal Summation
        phi1_modes=(Pl_theta.*Al2(:,frequency).*(jkr(:,frequency,dist)+...
            i*ykr(:,frequency,dist)));
        %phi1(1,frequency)=phi1l;
        phi_all(cnt_theta,frequency,dist)=phi1l;
        phi_all_modes(:,cnt_theta,frequency,dist)=phi1_modes;
       end
    end
end
clear jkr ykr Al2
phi_all(:,1)=0;
clc;disp(['!!!Done!!!']);

% TEMPOREL_PROCESS_WV_marston
% TEMPOREL_PROCESS_WV



%%%
% f1=1;
% f2=800000;
% df=200;
 f1=1;
 f2=100000;
 df=20;

Fs=df;
```

```
Fe=round(f2*10.5/Fs)*Fs;
Ts=1/Fe;N=1/Fs/Ts;T=N*Ts;

freq=[0:N-1]/N/Ts;
Ifreq=find(freq≥f1 & freq≤f2+df/10);

%%%%For Filtering
 Fmin=0;
 Fmax=f2/2;
%Fmin=1e3;
%Fmax=800e3;
Ifilter=find(freq(Ifreq)≥Fmin & freq(Ifreq)≤Fmax);

time=[0:N-1]*Ts;
c0=1500;zTARG=100;L=200;
for i=1:length(phi_all(:,1))
phi1=phi_all(i,:);
phi1(1)=0;
Kij=zeros(size(freq));
Kij(Ifreq(Ifilter))=conj(phi1(Ifilter)).*hanning(length(Ifreq(Ifilter))).';
%FP(:,jj).*Prod.*hanning(length(Ifreq));
P=real(ifft(Kij));

%freq_int1=[Fmin  Fmax];  [BB1,AA1]=butter(4,[freq_int1]/Fe*2);
%Pfil=filtfilt(BB1,AA1,P);
%%%%%%%%%%
%find(isnan(phi1)==1)
% figure(2);clf;%hold on
% %subplot(2,1,1)
% plot(time,P)
% title(['Receiver Angle ',int2str(sweep_theta(i)),' '])
% axis tight
```

```
% drawnow
% pause(.05)
 Irec=find(time>0.019&time≤0.029);
% Irec=find(time≥5e-3&time≤3e-2);
Pall(:,i)=P(Irec);%.*hanning(length(P(Irec))).';
% subplot(2,1,1);plot(time,P);
% subplot(2,1,2);plot(time(Irec),Pall(:,i));
% drawnow
% pause(.25)
IDX=find(abs(Pall(:,i))==max(abs(Pall(:,i))));
%P_spec(:,i)=Pall(:,i)*0;
%P_spec([IDX-50:IDX+50],i)=Pall([IDX-50:IDX+50],i);
end
clear IDX
% for i=1:length(P_spec(1,:))
%     [res,lags]=xcorr(P_spec(:,find(sweep_theta==180)),P_spec(:,i),'coeff'
%);
%     IDX=lags(find(res==max(res)));
%     Pall_sft(:,i)=circshift(Pall(:,i),IDX);
% end
% Pall_old=Pall;
% Pall=Pall_sft;
% clear Pall_sft IDX res lags
%     noise=wgn(length(Pall(:,1)),1,-90);
% for i=1:length(Pall(1,:))
%     Pall(:,i)=awgn(Pall(:,i),-5,'measured');
% end
%%2D plot
%MM=max(max(Pall));
%figure(1);clf;hold on
%imagesc(time(Irec),sweep_theta,20*log10(abs(Pall)'/MM))
%caxis([-60 0]);colorbar;
```

```
if 1==0
    %% WV ANALYSIS
%%%%^^^^^^^^^^^^^^^^^^^^^^^^^^^^^^^^^^^^^^^^^^^^^^^^^^^^^^^^^^^^^^^^^^^^^^^
%%%%^^^^^^^^^
%%%%%%%TIME-FREQUENCY ANALYSIS
%%%%%%%%%%%%%%%%%Time Frequency analysis;
      addpath('C:\Program Files\MATLAB\R2007a\toolbox\tftb-0.1\mfiles')
%%%%%%%%%%%%For Time Frequ Analysis
%%Select one angle
for Iang=1:length(sweep_theta)
    %pause
%Iang=find(sweep_theta==0);

%%Downsample to reduce the number of time samples to minimum necessary;
RATE=3;%round(Fe/Fmax/4);
FeNEW=Fe/RATE;
TsNEW=1/FeNEW;
DATA=decimate(Pall(:,Iang),RATE);%.*hanning(length(Pall(:,Iang))/RATE+1);
Nnew=length(DATA);
timeNEW=[0:Nnew-1]*TsNEW; % redefine time axis
Istart=min(find(DATA≥(max(DATA))))-50;  %[500:830]; %%Select a time-window
timeNEW=timeNEW-timeNEW(Istart);
% Istart=min(find(timeNEW≥0));  %[500:830]; %%Select a time -window
Npts=2^10;
IcentTF=[1:Npts]+Istart;
if max(IcentTF)>length(timeNEW);IcentTF=1:length(timeNEW);end
%IcentTF=[500:1000];
freq_int1=[Fmin,Fmax];
%%Make it even number-> remove last point;
if (mod(length(IcentTF),2)>0);IcentTF(end)=[];end;
TcentTF=timeNEW(IcentTF);
LENGTH1=length(TcentTF)/2;
```

```
Nc_TF=length(TcentTF);
freqC_TF=[0:Nc_TF-1]/Nc_TF/TsNEW;
   CC=DATA(IcentTF);%.*hanning(length(IcentTF));
%WV Analysis Function
        g=tftb_window(odd(LENGTH1/50),'hamming');%Time smoothing window
        h=tftb_window(odd(LENGTH1/1),'hamming');%Frequency smoothing window
        [Wig,Tc1,F1] =tfrspwv(CC+sqrt(-1)*hilbert(CC),[1:length(TcentTF)...
            ],LENGTH1,g,h);
        Wig=((Wig.'));%%each column is a frequency
        Fc1=[0:LENGTH1-1]/length(TcentTF)/TsNEW;
        If1=find(Fc1≥freq_int1(1) & Fc1≤freq_int1(2) );
        Fc2=Fc1;If2=If1;
        MMamp(Iang)=max(max(abs(Wig)));
        %WIG_all(:,:,Iang)=Wig(:,If1);
  %Plot Time Response
%       figure(Iang);clf
%       plot(timeNEW,DATA);axis([1.5e-4 TcentTF(end) min(DATA) max(DATA)]);

%       Scale=50; %%in DB
if 1==1 %Plot WV
figure(3);clf;%hold on
                %subplot(2,2,2);
          axes('Position',[0.2908 0.5838 0.6757 0.3405]);
          pcolor(TcentTF,Fc1(If1),20*log10(abs(Wig(:,If1).')/MMamp(Iang)));
          xlabel('Time','FontSize',20);ylabel('Frequency','FontSize',20);
          shading interp
          caxis([00 60]+10*log10(MMamp(Iang)));
          colorbar([0.1535 0.105 0.0357 0.3425])
        %       xlim(0.1/2*[-1 1])
                ylim(freq_int1)
                hold off
                axis tight
```

```
  title(['Smooth-Pseudo Wigner Ville : ',num2str(sweep_theta(Iang)),'deg'])
       % track(Iang,:)=ginput(1);
%Temporal Response
        %subplot(2,2,4);
        axes('Position',[0.2919 0.11 0.6746 0.3399]);
        plot(timeNEW,DATA);
        axis([TcentTF(1) TcentTF(end) min(DATA)/2 max(DATA)/2]);
%Frequency Response
        %subplot(2,2,1);
        axes('Position',[0.1047 0.584 0.09198 0.338]);
        plot(abs(fft(CC)),freqC_TF);
        set(gca,'XDir','reverse');
        xlim([0 max(abs(fft(CC)))]);ylim(freq_int1);
        ANI(Iang)=getframe(gcf);
% %Save Plots
%  direct = cd;
%  cd ..;cd iterations;
%  saveas(figure(3),[num2str(sweep_theta(Iang)),'deg_sphr','.fig'])
%  cd(direct)
end
end
end
% %% Plot Combination of all Angles
% for idx=1:length(WIG_all(1,1,:))
%     WIG_all(:,:,idx)=WIG_all(:,:,idx)/max(max(WIG_all(:,:,idx)));
% end
% wig_sum=sum(WIG_all(:,:,[30:180]),3);
% figure
% wig_log=20*log10((wig_sum.')/max(max(wig_sum)));
% pcolor(TcentTF,Fc1(If1),real(wig_log));
% shading interp
% caxis([-70 0]);colorbar
```

```
% ylim(freq_int1)
% axis tight
%% Plot Angle vs Time (Sinogram)
% figure
% pcolor(sweep_theta',time(Irec),20*log10(abs(Pall./max(max(Pall)))));
% shading interp
% caxis([-70 0])

%% Animation
% figure
% axes('Position',[0 0 1 1])
% movie(ANI,2,8)%playback 2 times at 8 frames/sec
%movie2avi(ANI,'test3.avi','fps',20,'compression', 'Cinepak')



%fichier_env = input('Enter Filename for Parameters ? ','s');
global file
fid = fopen( file, 'r' );
for l=1:3 fgetl(fid); end
s       = fscanf(fid,'%f',19);

%les indices 1, 2 et 3 signifient :
%            1 : milieu exterieur (ou milieu d'observation).
%            2 : la coque.
%            3 : le milieu interieur   la coque.
cl1        = s(1);
ct1        = s(2);
rho1       = s(3);
cl2        = s(4);
ct2        = s(5);
rho2       = s(6);
cl3        = s(7);
```

```
ct3         = s(8);
rho3        = s(9);
a           = s(10);%  Rayon extrieur de la sphre
rap         = s(11);%  Rapport des rayons
nb_mode     = s(12);%  Nombre de modes
alpha0      = s(13);%  Angle d'incidence(en deg) (dans le cas d'une coque
                    %    cylindrique.
theta       = s(14);%  Angle de reception(en deg)
r           = s(15);%  distance de reception (en m)   partir de la cible
z           = s(16);%  elevation du recepteur par rapport   l'axe
                    %    de l'incidence
                    %  normale(uniquement dans le cas d'une coque
                    %    cylindrique).
% Paramtres frquentiels
fmin = s(17);                 % Frquence min
fmax = s(18);                 % Frquence max
df   = s(19);                 % Pas d'chantillonnage

% Calcul intermediaire
b=rap*a;
theta_rd=pi*theta/180;
alpha0_rd = pi*alpha0/180;

% Affichage
info_milieu=['Outisde Medium Parameters :  [ rho=' num2str(rho1) ', cl=' num2str(cl1)
disp(info_milieu);

info_materiau=['Shell Material Parameters    :  [ rho=' num2str(rho2) ', cl=' num2st
disp(info_materiau);

info_milint  =['Inside Medium parameters :  [ rho=' num2str(rho3) ', cl=' num2str(cl
disp(info_milint);
```

```
% spherical Functions of Bessel + derived first + derived seconds.
%
%
% Definition:
% the spherical functions of Bessel of 1st and 2nd species of order m,
% noted respectively j_m and y_m, are the particular solutions of
% the diffentielle equation of Bessel written in spherical co-ordinates:
%
% f' ' + (2/z)*f' (z) + (1 m(m+1)/z^2)*f = 0; F = f(z), Z = alpha*r.
%
% syntax of the function: [ J, y, jp, YP, js, ys ] = bes_prim_sec_hs(M, x)
%
% M: a vector (column preferably) containing the orders
% whole sussecssifs ' m_i' of the spherical functions of Bessel.
% X: a scalar % J: vector column containing the functions of Bessel of 1ere
% species of orders ' m_i' as in point X, j_m_i(x).
% y: vector column containing the values of the functions of
% Bessel spherical of 2nd species of orders ' m_i' at the point
% X, y_m_i(x). % jp: vector column containing the values of derived from
% spherical functions of Bessel of 1ere species of orders ' m_i' to
% not X, I _m_i(x).
% YP: vector column containing the values of derived from
% spherical functions of Bessel of 2nd species of orders ' m_i' to
% not X, y' _m_i(x). % js: vector column containing the values of derived
% seconds from the functions of Bessel of 1ere species of orders
% ' m_i' as in point X, I ' _m_i(x).
% ys: vector column containing the values of derived
% seconds from the functions of Bessel of 2nd species of orders
% ' m_i' as in point X, y' ' _m_i(x).

function [j,y,jp,yp,js,ys]= bes_prim_sec_hs(M,x)
[m,n]=size(M);
```

```
if n > 1 & m > 1
  disp('Error, M must be a vector column');
end

if n > 1 | m == 1,
  M=M';
end

ord=[M ; max(M)+1];
long=length(ord);

% Formulas binding the spherical functions of Bessel to the functions of
% Bessel normals (valid for the functions of 1st species like
% for the functions of 2nd species): % j_m(z) = sqrt(pi/(2z))*J_(m+1/2)(z)
% j(en miniscule): spherical function of Bessel
% J(en capital letter): normal function of Bessel
j_temporaire=sqrt(pi/(2*x))*besselj((ord+0.5), x);
y_temporaire=sqrt(pi/(2*x))*bessely((ord+0.5), x);
j=j_temporaire(1:long-1);
y=y_temporaire(1:long-1);

% Relation of recurrence for the derivative 1st:
% z*j' _m(z) = m*j_m(z)-z*j_(m+1)(z)
% This formula is valid also for y_m(z).
aux1=ord(1:long-1)./x;
jp=aux1.*j-j_temporaire(2:long);
yp=aux1.*y-y_temporaire(2:long);
% Relation of recurrence for the derivative second:
% z^2*j' ' _m(z) = (m(m+1)-z^2)*j_m(z)-2*z*j' _m(z)
% This formula is valid also for y_m(z).
aux=((M.*(M+1))./x.^2)-1;
```

```
js=-(2*jp./x)+aux.*j;
ys=-(2*yp./x)+aux.*y;


%  Fonctions de  Bessel sphriques + drives premires + drives secondes.
%
%   Definition:
%   Les fonctions de Bessel sphriques de 1ere et 2eme espce d'ordre m,
%   notes respectivement j_m et y_m, sont les solutions particulires de
%   l'quation diffentielle de Bessel crite en coordonnes sphriques:
%
%       f''+ (2/z)*f'(z) + (1- m(m+1)/z^2)*f = 0  ;  f = f(z), z = alpha*r.
%
%   syntaxe de la fonction: [j,y,jp,yp,js,ys]= bes_prim_sec_hs(M,x)
%
%   M     : un vecteur (colonne de prfrence) contenant les ordres
%           entiers sussecssifs 'm_i' des fonctions de Bessel sphriques.
%   x     : un scalaire.
%   j     : vecteur colonne contenant les fonctions de Bessel de 1ere
%           espce d'ordres 'm_i' au point x, j_m_i(x).
%   y     : vecteur colonne contenant les valeurs des fonctions de
%           Bessel sphriques de 2eme espce d'ordres 'm_i' au point
%           x,y_m_i(x).
%   jp    : vecteur colonne contenant les valeurs des drives des
%           fonctions de Bessel sphriques de 1ere espce d'ordres 'm_i' au
%           point x, j'_m_i(x).
%   yp    : vecteur colonne contenant les valeurs des drives des
%           fonctions de Bessel sphriques de 2eme espce d'ordres 'm_i' au
%           point x, y'_m_i(x).
%   js    : vecteur colonne contenant les valeurs des drives
%           secondes des fonctions de Bessel de 1ere espce d'ordres
%           'm_i' au point x, j''_m_i(x).
```

```
%   ys    : vecteur colonne contenant les valeurs des drives
%           secondes des fonctions de Bessel de 2eme espce d'ordres
%           'm_i' au point x, y''_m_i(x).

function [j,y,jp,yp,js,ys]= bes_prim_sec_hs(M,x)
[m,n]=size(M);

if n > 1 & m > 1
  disp('Erreur,M doit tre un vecteur colonne.');
end

if n > 1 | m == 1,
  M=M';
end

ord=[M ; max(M)+1];
long=length(ord);

   % Formules liant les fonctions de Bessel sphriques aux fonctions de
   % Bessel normales (valables pour les fonctions de 1ere espces comme
   % pour les fonctions de 2eme espce):
   %    j_m(z)= sqrt(pi/(2z))*J_(m+1/2)(z)
   %  j(en miniscule): fonction de Bessel sphrique
   %  J(en majuscule): fonction de Bessel normale

j_temporaire=sqrt(pi/(2*x))*besselj((ord+0.5),x);
y_temporaire=sqrt(pi/(2*x))*bessely((ord+0.5),x);
j=j_temporaire(1:long-1);
y=y_temporaire(1:long-1);

       % Relation de rcurrence pour la drive 1ere:
       %   z*j'_m(z) = m*j_m(z)-z*j_(m+1)(z)
```

```
       % Cette formule est valable aussi pour y_m(z).

aux1=ord(1:long-1)./x;
jp=aux1.*j-j_temporaire(2:long);
yp=aux1.*y-y_temporaire(2:long);


       % Relation de rcurrence pour la d r i v e seconde:
       %   z^2*j''_m(z) = (m(m+1)-z^2)*j_m(z)-2*z*j'_m(z)
       % Cette formule est valable aussi pour y_m(z).

aux=((M.*(M+1))./x.^2)-1;
js=-(2*jp./x)+aux.*j;
ys=-(2*yp./x)+aux.*y;


%    Polynome de legendre de degre zero d'ordre deg.
%
%    Le but de ce programme est de calculer les polynomes de Legendre.
%
%     P[n+1](z)=1/(n+1)*((2n+1)*z*P[n](z)-n*P[n-1](z)
%     deg et x sont des scalaires .
%     p un vecteur de dim deg+1

function [p] = genpol(deg,x)

%on initialise la relation de recurrence avec P[0]=p(1)
p(1) = 1;

%Si le degre du polynome est superieur   0, on calcule P[1]=p(2)
if deg > 0,
    p(2) = x;
```

```
%Si le degre est superieur   2, on peut commencer la rcurrence.
    if deg ≥ 2,

        for l = 3:deg+1
        p(l) = ((2*l-3)*x*p(l-1)-(l-2)*p(l-2))/(l-1);
        end

    end

end
```

APPENDIX B

MODAL EXPANSION COEFFICIENTS

$$A_l^{\mathrm{I}} = -i^l(2l+1)\frac{\begin{vmatrix} a_1 & \alpha_{12} & \alpha_{13} & \alpha_{14} & \alpha_{15} & 0 \\ a_2 & \alpha_{22} & \alpha_{23} & \alpha_{24} & \alpha_{25} & 0 \\ 0 & \alpha_{32} & \alpha_{33} & \alpha_{34} & \alpha_{35} & 0 \\ 0 & \alpha_{42} & \alpha_{43} & \alpha_{44} & \alpha_{45} & \alpha_{46} \\ 0 & \alpha_{52} & \alpha_{53} & \alpha_{54} & \alpha_{55} & \alpha_{56} \\ 0 & \alpha_{62} & \alpha_{63} & \alpha_{64} & \alpha_{65} & 0 \end{vmatrix}}{\begin{vmatrix} \alpha_{11} & \alpha_{12} & \alpha_{13} & \alpha_{14} & \alpha_{15} & 0 \\ \alpha_{21} & \alpha_{22} & \alpha_{23} & \alpha_{24} & \alpha_{25} & 0 \\ 0 & \alpha_{32} & \alpha_{33} & \alpha_{34} & \alpha_{35} & 0 \\ 0 & \alpha_{42} & \alpha_{43} & \alpha_{44} & \alpha_{45} & \alpha_{46} \\ 0 & \alpha_{52} & \alpha_{53} & \alpha_{54} & \alpha_{55} & \alpha_{56} \\ 0 & \alpha_{62} & \alpha_{63} & \alpha_{64} & \alpha_{65} & 0 \end{vmatrix}} \tag{6a}$$

for $l \geqq 1$, and

$$A_0^{\mathrm{I}} = -\frac{\begin{vmatrix} a_1 & \alpha_{12} & \alpha_{14} & 0 \\ a_2 & \alpha_{22} & \alpha_{24} & 0 \\ 0 & \alpha_{42} & \alpha_{44} & \alpha_{46} \\ 0 & \alpha_{52} & \alpha_{54} & \alpha_{56} \end{vmatrix}}{\begin{vmatrix} \alpha_{11} & \alpha_{12} & \alpha_{14} & 0 \\ \alpha_{21} & \alpha_{22} & \alpha_{24} & 0 \\ 0 & \alpha_{42} & \alpha_{44} & \alpha_{46} \\ 0 & \alpha_{52} & \alpha_{54} & \alpha_{56} \end{vmatrix}}. \tag{6b}$$

Using the abbreviations $x=kR$, $x_L=k_LR$, $x_T=k_TR$, $y=k(R-\Delta)$, $y_L=k_L(R-\Delta)$, and $y_T=k_T(R-\Delta)$, the elements of the determinants are given by

$$a_1 = j_l(x)\rho_{\mathrm{I}}/\rho_{\mathrm{II}}, \tag{7a}$$

$$a_2 = x j_l'(x), \tag{7b}$$

$$\alpha_{11} = h_l^{(1)}(x)\rho_{\mathrm{I}}/\rho_{\mathrm{II}}, \tag{7c}$$

$$\alpha_{21} = x h_l^{(1)\prime}(x), \tag{7d}$$

$$\alpha_{12} = [\lambda_{\mathrm{II}} j_l(x_L) - 2\mu_{\mathrm{II}} j_l''(x_L)]/(\lambda_{\mathrm{II}} + 2\mu_{\mathrm{II}}), \tag{7e}$$

Figure 21: Modal Expansion coefficients taken from Eq.(6a) and Eq. (6b) in Goodman and Stern [6].

$$\alpha_{22}=x_L j_l'(x_L), \tag{7f}$$

$$\alpha_{12}=2[x_L j_l'(x_L)-j_l(x_L)], \tag{7g}$$

$$\alpha_{42}=[\lambda_{II} j_l(y_L)-2\mu_{II} j_l''(y_L)]/(\lambda_{II}+2\mu_{II}), \tag{7h}$$

$$\alpha_{82}=y_L j'(y_L), \tag{7i}$$

$$\alpha_{62}=2[y_L j_l'(y_L)-j_l(y_L)], \tag{7j}$$

$$\alpha_{13}=-2l(l+1)x_T^{-2}[x_T j_l'(x_T)-j_l(x_T)], \tag{7k}$$

$$\alpha_{23}=l(l+1)j_l(x_T), \tag{7l}$$

$$\alpha_{33}=x_T^2 j_l''(x_T)+(l+2)(l-1)j_l(x_T), \tag{7m}$$

$$\alpha_{43}=-2l(l+1)y_T^{-2}[y_T j_l'(y_T)-j_l(y_T)], \tag{7n}$$

$$\alpha_{63}=l(l+1)j_l(y_T), \tag{7o}$$

$$\alpha_{63}=y_T^2 j_l''(y_T)+(l+2)(l-1)j_l(y_T), \tag{7p}$$

$$\alpha_{14}=[\lambda_{II} n_l(x_L)-2\mu_{II} n_l''(x_L)]/(\lambda_{II}+2\mu_{II}), \tag{7q}$$

$$\alpha_{24}=x_L n_l'(x_L), \tag{7r}$$

$$\alpha_{34}=2[x_L n_l'(x_L)-n_l(x_L)], \tag{7s}$$

$$\alpha_{44}=[\lambda_{II} n_l(y_L)-2\mu_{II} n_l''(y_L)]/(\lambda_{II}+2\mu_{II}), \tag{7t}$$

$$\alpha_{54}=y_L n_l'(y_L), \tag{7u}$$

$$\alpha_{64}=2[y_L n_l'(y_L)-n_l(y_L)], \tag{7v}$$

$$\alpha_{15}=-2l(l+1)x_T^{-2}[x_T n_l'(x_T)-n_l(x_T)], \tag{7w}$$

$$\alpha_{25}=l(l+1)n_l(x_T), \tag{7x}$$

$$\alpha_{35}=x_T^2 n_l''(x_T)+(l+2)(l-1)n_l(x_T), \tag{7y}$$

$$\alpha_{45}=-2l(l+1)y_T^{-2}[y_T n_l'(y_T)-n_l(y_T)], \tag{7z}$$

$$\alpha_{55}=l(l+1)n_l(y_T), \tag{7aa}$$

$$\alpha_{65}=y_T^2 n_l''(y_T)+(l+2)(l-1)n_l(y_T), \tag{7bb}$$

$$\alpha_{46}=j_l(y)\rho_{II}/\rho_{II}, \tag{7cc}$$

$$\alpha_{56}=y j_l'(y). \tag{7dd}$$

Figure 22: Additional details of Modal Expansion coefficients taken from Eq.(6a) and Eq. (6b) in Goodman and Stern [6].

REFERENCES

[1] Achenbach, J., *Wave Propagation in Elastic Solids*. Elsevier Science Publishers B.V., 1975.

[2] Blondel, P. and Caiti, A., *Buried Waste in the Seabed: Acoustic Imaging and Bio-toxicity*. Springer, 2007.

[3] Cohen, L., *Time Frequency Analysis: Theory and Applications*. New Jersey: Prentice Hall PTR, 1995.

[4] Felsen, L. B., Ho, J. M., and Lu, I. T., "Three-dimensional green's function for fluid-loaded thin elastic cylindrical shell: Alternative representations and ray acoustic forms," *The Journal of the Acoustical Society of America*, vol. 87, no. 2, pp. 554–569, 1990.

[5] Flandrin, P., Sageloli, J., Sessarego, J., and Zakharia, M., "Application of time-frequency analysis to the characterization of surface waves on elastic targets," *Acoustics Letters*, vol. 10, no. 2, pp. 23–28, 1986.

[6] Goodman, R. R. and Stern, R., "Reflection and transmission of sound by elastic spherical shells," *The Journal of the Acoustical Society of America*, vol. 34, no. 3, pp. 338–344, 1962.

[7] Ho, J.-M., "Near-field ray acoustic response of submerged elastic spherical shells," *The Journal of the Acoustical Society of America*, vol. 96, no. 1, pp. 525–535, 1994.

[8] Kaduchak, G. and Marston, P. L., "Backscattering of chirped bursts by a thin spherical shell near the coincidence frequency," *The Journal of the Acoustical Society of America*, vol. 93, no. 5, pp. 2700–2706, 1993.

[9] Kargl, S. G. and Marston, P. L., "Observations and modeling of the backscattering of short tone bursts from a spherical shell: Lamb wave echoes, glory, and axial reverberations," *The Journal of the Acoustical Society of America*, vol. 85, no. 3, pp. 1014–1028, 1989.

[10] LePage, K. and Schmidt, H., "Bistatic synthetic aperture imaging of proud and buried targets from an auv," *Oceanic Engineering, IEEE Journal of*, vol. 27, pp. 471 – 483, jul 2002.

[11] Li, W., Liu, G. R., and Varadan, V. K., "Estimation of radius and thickness of a thin spherical shell in water using the midfrequency enhancement of a short tone burst response," *The Journal of the Acoustical Society of America*, vol. 118, no. 4, pp. 2147–2153, 2005.

[12] Lucifredi, I. and Schmidt, H., "Subcritical scattering from buried elastic shells," *The Journal of the Acoustical Society of America*, vol. 120, no. 6, pp. 3566–3583, 2006.

[13] Magand, F. and Chevret, P., "Time frequency analysis of energy distribution for circumferential waves on cylindrical elastic shells," *Acta Acustica united with Acustica*, vol. 82, pp. 707–716, October 1996.

[14] Marston, P. L. and Sun, N. H., "Resonance and interference scattering near the coincidence frequency of a thin spherical shell: An approximate ray synthesis," *The Journal of the Acoustical Society of America*, vol. 92, no. 6, pp. 3315–3319, 1992.

[15] Marston, P. L. and Sun, N. H., "Backscattering near the coincidence frequency of a thin cylindrical shell: Surface wave properties from elasticity theory and an approximate ray synthesis," *The Journal of the Acoustical Society of America*, vol. 97, no. 2, pp. 777–783, 1995.

[16] Mitchell, S. and Pitt, S., "Bistatic sas imaging studies," in *Proceedings of the Institute of Acoustics, London*, vol. 4, 9 2006.

[17] Morse, S. F. and Marston, P. L., "Backscattering of transients by tilted truncated cylindrical shells: Time-frequency identification of ray contributions from measurements," *The Journal of the Acoustical Society of America*, vol. 111, no. 3, pp. 1289–1294, 2002.

[18] Rose, J. L., *Ultrasonic Waves in Solid Media*. New York: Cambridge University Press, 1999.

[19] Sammelmann, G. S., Trivett, D. H., and Hackman, R. H., "The acoustic scattering by a submerged, spherical shell. i: The bifurcation of the dispersion curve for the spherical antisymmetric lamb wave," *The Journal of the Acoustical Society of America*, vol. 85, no. 1, pp. 114–124, 1989.

[20] Son, J., Thomas, G., and B.C., F., *Range-Doppler Radar Imaging and Motion Compensation*. Boston: Artech House, 2001.

[21] Sun, N. H. and Marston, P. L., "Ray synthesis of leaky lamb wave contributions to backscattering from thick cylindrical shells," *The Journal of the Acoustical Society of America*, vol. 91, no. 3, pp. 1398–1402, 1992.

[22] Talmant, M., Uberall, H., Miller, R. D., Werby, M. F., and Dickey, J. W., "Lamb waves and fluid-borne waves on water-loaded, air-filled thin spherical shells," *The Journal of the Acoustical Society of America*, vol. 86, no. 1, pp. 278–289, 1989.

[23] Tesei, A., Fox, W. L. J., Maguer, A., and Lovik, A., "Target parameter estimation using resonance scattering analysis applied to air-filled, cylindrical

shells in water," *The Journal of the Acoustical Society of America*, vol. 108, no. 6, pp. 2891–2900, 2000.

[24] Tesei, A., Maguer, A., Fox, W. L. J., Lim, R., and Schmidt, H., "Measurements and modeling of acoustic scattering from partially and completely buried spherical shells," *The Journal of the Acoustical Society of America*, vol. 112, no. 5, pp. 1817–1830, 2002.

[25] Uberall, H., Gaunaurd, G., and Murphy, J. D., "Acoustic surface wave pulses and the ringing of resonances," *The Journal of the Acoustical Society of America*, vol. 72, no. 3, pp. 1014–1017, 1982.

[26] Van Trees, H. L., *Detection, Estimation, and Modulation Theory: Optimum Array Processing*. USA: Wiley-Interscience, 2002.

[27] Weiss, L., "Wavelets and wideband correlation processing," *Signal Processing Magazine, IEEE*, vol. 11, pp. 13 –32, jan 1994.

[28] Williams, K. L., Kargl, S. G., Thorsos, E. I., Burnett, D. S., Lopes, J. L., Zampolli, M., and Marston, P. L., "Acoustic scattering from a solid aluminum cylinder in contact with a sand sediment: Measurements, modeling, and interpretation," *The Journal of the Acoustical Society of America*, vol. 127, no. 6, pp. 3356–3371, 2010.

[29] Zakharia, M. and Sessarego, J., "Sonar target classification using a coherent echo processing," in *Acoustics, Speech, and Signal Processing, IEEE International Conference on ICASSP '82.*, vol. 7, pp. 331 – 334, may 1982.

[30] Zakharia, M. E., Flandrin, P., Sessarego, J., and Sagloli, J., "Analyse temps-frquence applique la caractrisation acoustique de cibles," *J. Acoustique*, vol. 1, pp. 185–188, 1988.

[31] Zakharia, M. E. and Chevret, P., "Neural network approach for inverting velocity dispersion; application to sediment and to sonar target characterization," *Inverse Problems*, vol. 16, no. 6, p. 1693, 2000.

[32] Zakharia, M., Magand, F., Sessarego, J.-P., and Sagloli, J., *Application of time-frequency analysis to the characterization of acoustical scattering (Chapter 7 of Acoustic interaction with submerged elastic structures)*. New Jersey: Word Scientific Publications, 2001.

[33] Zakharia, M. and Sessarego, J.-P., "Application of time-frequency analysis to non destructive evaluation (n.d.e.)," in *Proceedings of The IEEE Ultrasonics Symposium*, vol. 2, (Lake Buena Vista, Florida), pp. 809–818, 12 1991.

[34] Zhang, L. G., Sun, N. H., and Marston, P. L., "Midfrequency enhancement of the backscattering of tone bursts by thin spherical shells," *The Journal of the Acoustical Society of America*, vol. 91, no. 4, pp. 1862–1874, 1992.

[35] Zhang, P. and Geers, T. L., "Excitation of a fluid-filled, submerged spherical shell by a transient acoustic wave," *The Journal of the Acoustical Society of America*, vol. 93, no. 2, pp. 696–705, 1993.